Ocean Modelling 100 (2016) 141–161

Contents lists available at ScienceDirect

Ocean Modelling

journal homepage: www.elsevier.com/locate/ocemod

An assessment of the Arctic Ocean in a suite of interannual CORE-II simulations. Part III: Hydrography and fluxes

Mehmet Ilıcak[a,*], Helge Drange[b,c], Qiang Wang[d], Rüdiger Gerdes[d], Yevgeny Aksenov[e], David Bailey[f], Mats Bentsen[a], Arne Biastoch[g], Alexandra Bozec[h], Claus Böning[g], Christophe Cassou[i], Eric Chassignet[h], Andrew C. Coward[e], Beth Curry[j], Gokhan Danabasoglu[f], Sergey Danilov[d], Elodie Fernandez[i], Pier Giuseppe Fogli[k], Yosuke Fujii[l], Stephen M. Griffies[m], Doroteaciro Iovino[k], Alexandra Jahn[f,s], Thomas Jung[d], William G. Large[f], Craig Lee[j], Camille Lique[n,u], Jianhua Lu[h], Simona Masina[k,r], A.J. George Nurser[e], Christina Roth[g], David Salas y Mélia[o], Bonita L. Samuels[m], Paul Spence[p,q], Hiroyuki Tsujino[l], Sophie Valcke[i], Aurore Voldoire[o], Xuezhu Wang[d], Steve G. Yeager[f]

[a] *Uni Research Climate, Bjerknes Centre for Climate Research, Bergen, Norway*
[b] *Geophysical Institute, University of Bergen, Bergen, Norway*
[c] *Bjerknes Centre for Climate Research, Bergen, Norway*
[d] *Alfred Wegener Institute, Helmholtz Centre for Polar and Marine Research (AWI), Bremerhaven, Germany*
[e] *National Oceanography Centre (NOC), Southampton SO14 3ZH, UK*
[f] *National Center for Atmospheric Research (NCAR), Boulder, CO, USA*
[g] *GEOMAR Helmholtz Centre for Ocean Research, Kiel, Germany*
[h] *Center for Ocean-Atmospheric Prediction Studies (COAPS), Florida State University, Tallahassee, FL, USA*
[i] *Unité de Recherche Associée 1875, Centre National de la Recherche Scientifique/Centre Européen de Recherche et de Formation Avancée en Calcul Scientifique, Toulouse, France*
[j] *Applied Physics Laboratory, University of Washington, Seattle, WA, USA*
[k] *Centro Euro-Mediterraneo sui Cambiamenti Climatici (CMCC), Bologna, Italy*
[l] *Meteorological Research Institute (MRI), Japan Meteorological Agency, Tsukuba, Japan*
[m] *NOAA Geophysical Fluid Dynamics Laboratory (GFDL), Princeton, NJ, USA*
[n] *Department of Earth Sciences, University of Oxford, Oxford, UK*
[o] *Centre National de Recherches Météorologiques (CNRM), Toulouse, France*
[p] *ARC Centre of Excellence for Climate System Science, University of New South Wales, Sydney, New South Wales, Australia*
[q] *Climate Change Research Centre, University of New South Wales, Sydney, Australia*
[r] *Istituto Nazionale di Geofisica e Vulcanologia (INGV), Bologna, Italy*
[s] *Department of Atmopheric and Oceanic Sciences, Institute of Arctic and Alpine Research, University of Colorado Boulder, Boulder, CO, USA*
[t] *Laboratoire de Physique des Océans, Ifremer, Brest, France*

ARTICLE INFO

Article history:
Received 28 May 2015
Revised 11 January 2016
Accepted 6 February 2016
Available online 27 February 2016

Keywords:
Arctic Ocean
Atlantic Water
St. Anna Trough
Density currents
CORE-II atmospheric forcing

ABSTRACT

In this paper we compare the simulated Arctic Ocean in 15 global ocean–sea ice models in the framework of the Coordinated Ocean-ice Reference Experiments, phase II (CORE-II). Most of these models are the ocean and sea-ice components of the coupled climate models used in the Coupled Model Intercomparison Project Phase 5 (CMIP5) experiments. We mainly focus on the hydrography of the Arctic interior, the state of Atlantic Water layer and heat and volume transports at the gateways of the Davis Strait, the Bering Strait, the Fram Strait and the Barents Sea Opening. We found that there is a large spread in temperature in the Arctic Ocean between the models, and generally large differences compared to the observed temperature at intermediate depths. Warm bias models have a strong temperature anomaly of inflow of the Atlantic Water entering the Arctic Ocean through the Fram Strait. Another process that is not represented accurately in the CORE-II models is the formation of cold and dense water, originating on the eastern shelves. In the cold bias models, excessive cold water forms in the Barents Sea and spreads

* Corresponding author. Tel.: +17863251094.
E-mail address: mehmet.ilicak@noaa.gov, mehmet.ilicak@uni.no (M. Ilıcak).

http://dx.doi.org/10.1016/j.ocemod.2016.02.004

into the Arctic Ocean through the St. Anna Through. There is a large spread in the simulated mean heat and volume transports through the Fram Strait and the Barents Sea Opening. The models agree more on the decadal variability, to a large degree dictated by the common atmospheric forcing. We conclude that the CORE-II model study helps us to understand the crucial biases in the Arctic Ocean. The current coarse resolution state-of-the-art ocean models need to be improved in accurate representation of the Atlantic Water inflow into the Arctic and density currents coming from the shelves.

1. Introduction

The Arctic Basin has traditionally been considered as slowly adjusting to long-term variations in the local atmospheric forcing or the input of Atlantic Water (AW) through the Fram Strait and the Barents Sea Opening and Pacific Water (PW) through the Bering Strait (e.g., Rudels, 1987, 2015). Observations of hydrography, circulation and sea ice cover during the recent decades show, however, a highly dynamic ocean basin (Polyak et al., 2010; Polyakov et al., 2012; Haine et al., 2015). These changes directly influence the coastal geography and the human settlements, infrastructures, transportation and exploitation of natural resources in the Arctic, in addition to altering the marine and terrestrial ecosystems, including fisheries and the cycling of carbon (e.g., ACIA, 2005; Hinzman et al., 2013).

Through the sustained poleward transport of atmospheric heat and moisture, the climate of the Arctic is highly influenced by the climate at lower latitudes. Dickson et al. (2000) described the effect of the North Atlantic Oscillation (NAO) on the Arctic region. Positive NAO phase increases the amount and temperature of the AW inflow to the Arctic Ocean via the Fram Strait and the Barents Sea. The extent to which changes in the Arctic are already influencing lower latitudes is, however, being debated with somewhat conflicting views (e.g., Blüthgen et al., 2012; Cohen et al., 2014; Mori et al., 2014; Wallace et al., 2014). Irrespective of these discussions, there are potentially severe consequences of an Arctic region in transition, notably related to the formation of a part of the deep water masses of the Atlantic Thermohaline Circulation (Eldevik and Nilsen, 2013), large-scale changes in the atmospheric circulation (e.g., Kug et al., 2015), accelerated melting of the Greenland ice sheet (e.g. Applegate et al., 2014; Koenig et al., 2014), and thawing of the extensive permafrost regions bordering the Arctic Ocean (e.g. O'Connor et al., 2010).

Robust assessments of naturally occurring variations and long-term changes in the climate of the Arctic require a diversity of thoroughly tested and verified climate models. The complexity – and to some extent uniqueness – of physical and thermodynamic processes taking place in the Arctic Ocean, coupled with the sparseness of long-term observations, make modeling the Arctic Ocean a challenging task. This is, as an example, exemplified by the large model spread in sea ice extent and thickness simulated by the state-of-the-art global climate models (Flato et al., 2013). The potential for interannual to decadal predictability of the Arctic climate is also heavily influenced – and likely restricted – by the sparsity of available observations, the complexity of the region, and the rapid, large-scale changes taking place.

For more than a decade, the Arctic Ocean Model Intercomparison Project (AOMIP; Proshutinsky and Kowalik, 2007; Proshutinsky et al., 2011) and its continuation named the Forum for Arctic Modeling and Observational Synthesis (FAMOS, http://www.whoi.edu/projects/famos/), have identified and analyzed systematic errors and subsequently improved Ocean General Circulation Models (OGCMs) for the Arctic Ocean. The model runs done in AOMIP were mostly performed with uncoordinated atmospheric forcing and with varying model set-up, model domains and model physics (e.g. Jahn et al., 2012). The spin-up and model integration time were generally short, typically lasting for less than a century, mainly because of the use of regional model domains with prescribed boundary conditions. The scientific outcome of AOMIP has nevertheless been substantial, with model improvements being implemented in global-scale OGCMs.

In this and two accompanying papers (Wang et al., 2016a; 2016b), the hydrography, liquid and solid fresh water budgets, and the volume and heat transports into and out of the Arctic Ocean are examined in global-scale, state-of-the-art OGCMs by applying the Coordinated Ocean-ice Reference Experiments (CORE-II) interannual forcing protocol (Griffies et al., 2009, 2012). In addition to a common forcing protocol, all of the models in CORE-II are run for 300 years or more. Fifteen models are included in the presented analysis, including level (geopotential), isopycnic (density) and hybrid coordinate models. In the analysis presented here, we focus primarily on two aspects: (i) the mean ocean state for the period 1978–2007; and (ii) the temporal evolution of the volume and heat fluxes into the Arctic Ocean from the Fram Strait, the Davis Strait, the Bering Strait and the Barents Sea.

In earlier modeling studies, Holloway et al. (2007) and Karcher et al. (2007) documented a rather wide scatter in the simulated hydrography in the AOMIP-models. One of their central finding was that most models simulated a progressive thickening of the sub-surface Atlantic Layer. It was speculated that numerical mixing caused by the advection operator might be the reason for this model bias. Holloway et al. (2007) tested the second order moment method of Prather, 1986 and obtained an improved representation of the Atlantic Inflow Water. Ten years later, we find that state-of-the-art global ocean models still suffer from a deepening of the AW. We also find that exchange processes and gravity currents along the western Arctic shelf breaks are other crucial problems in the current generation of global-scale OGCMs.

The paper is organized as follows: a summary of the water masses and circulation in the Arctic Ocean is given in Section 3. The models analyzed and the CORE-II surface forcing are briefly described in Section 4. We explain main biases on the hydrography with particular focus on the AW layer in the Arctic Ocean in Section 5. We summarize our conclusions and provide some discussions in Section 6.

2. Background

With an averaged depth of 1038 m and an area of 14.06×10^6 km^2, the Arctic Ocean is the smallest and shallowest of the five ocean basins. The ocean is enclosed by the Eurasian and the North American landmasses (Fig. 1), it is connected with the Nordic Seas through the Fram Strait and the Barents Sea Opening, and with the Pacific Ocean through the Bering Strait. The Arctic Ocean is also connected to the Labrador Sea through the straits of the Canadian Arctic Archipelago.

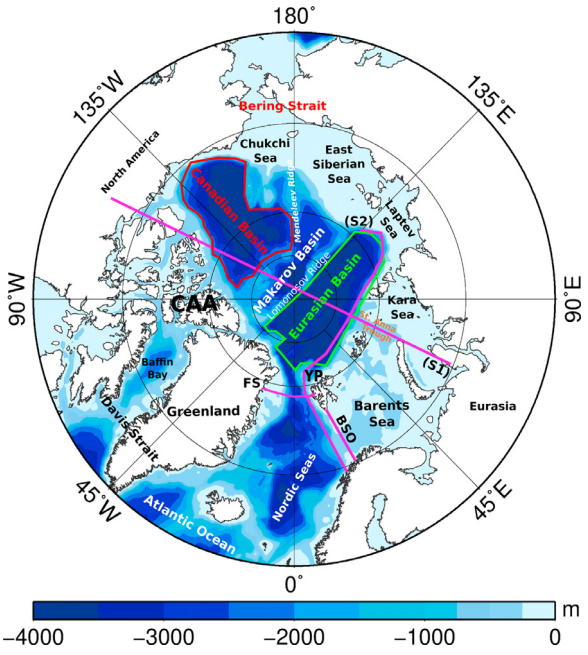

Fig. 1. Arctic Ocean bottom topography [m] from ETOPO2v2 dataset (http://www.ngdc.noaa.gov/mgg/fliers/06mgg01.html). Four different sections are shown in magenta; (i) a section along 70°E – North Pole – 110°W (S1), (ii) a section along the pathway of the AW through the Fram Strait (S2), (iii) the Fram Strait section (FS), and (iv) the southern Barents Sea Opening section (BSO). The Eurasian and the Canadian Basins are outlined in green and red lines, respectively. YP is the Yermak Plateau and CAA is the Canadian Arctic Archipelago. (For interpretation of the references to color in this figure legend, the reader is referred to the web version of this article.)

The Arctic Ocean is mainly covered by sea ice in winter but with more than half of the area ice-free during the permanently sunlit summer season. Exchanges of water masses take place through the narrow and shallow Bering Strait (+0.8 Sv, where 1 Sv= 10^6 m^3 s^{-1}; positive transport values imply net transport into the Arctic, Roach et al., 1995; Woodgate and Aagaard, 2005), through the relatively deep Fram Strait (-2 ± 2.7 Sv, Schauer et al., 2008), through the shallow and wide Barents Sea Opening (+2 Sv, Skagseth et al., 2008), and through several narrow openings in the Canadian Archipelago (about −1.6 Sv, Curry et al., 2014). An additional river input of about +0.1 Sv (McClelland et al., 2006) feeds fresh water into the basin.

Arctic Ocean is a deep basin with extensive continental shelves, notably along the European and the Siberian coasts. The basin is split into three sub-basins by the Lomonosov Ridge extending from North Greenland across the North Pole to Siberia, and the Mendeleev Ridge on the Pacific side of the Lomonosov Ridge. The three ocean sub-basins are named, in order from the European coast and with typical depths indicated, the Eurasian Basin (4000–4500 m; green outline in Fig. 1), the Makarov Basin (2000–2500 m), and the Canadian Basin (3000–3500 m; red outline in Fig. 1).

The Arctic Ocean modeling is challenging in several aspects (Rudels, 2012). The ocean circulation is complex with a small Rossby deformation radius due to its high latitude and, for shelf and sub-surface waters, relatively weak stratification (Nurser and Bacon, 2014). Formation and melting of sea ice, leading to exchange of salt and freshwater at different locations due to sea ice transport, are commonly found in the region. The formation of sea ice leads to cascading, dense brine-enriched waters off the shelves, linking the surface with the abyss (Midttun, 1985; Blindheim, 1989; Skogseth et al., 2005). Furthermore, the Arctic Ocean receives large amounts of fresh water from the neighboring land masses, and particularly the Eurasian rivers (Peterson et al., 2002; Zhang et al., 2013) contribute to a thick near-surface halocline (Steele and Boyd, 1998; Haine et al., 2015). Another critical process is the subduction of relatively warm and saline AW in and near the Fram Strait (Mauritzen, 1996; Price, 2001), contributing to the prominent layering of water masses in the upper part of the water column.

For detailed assessment of observed and modeled liquid and solid fresh water budgets, the readers are referred to Haine et al. (2015) and (Wang et al., 2016a; 2016b).

3. Description of observed Arctic Water masses and their pathways

In the following, the major water masses and their pathways in the Arctic Ocean are described based on annual fields derived from the PHC3.0 climatology (Steele et al., 2001). Although observation-based, one should remember that biases in the seasonal and geographical sampling of the water masses in the region may lead to an overly smooth temperature distribution, particularly on or near the ocean shelves and in the vicinity of sea ice. Four distinctive water masses are found in the Arctic (e.g., Jones, 2001; Rudels et al., 2013; Pemberton et al., 2015): at top, the Polar Mixed Layer (PML) is found. Below the PML and above the deeper warm AW, the Upper Polar Deep Water is located. Then the warm and (relatively) saline AW is found. And finally, the bottom deep water (depth > 2500 m) resides below the AW.

The relatively warm continuation of the North Atlantic current flows northward along the Norwegian coast as the Norwegian Atlantic Current (NwAC), consisting of a western and an eastern branch (Orvik, 2002). When approaching the Barents Sea Opening, the eastern branch of NwAC bifurcates with one branch flowing towards the Fram Strait and the other branch entering the Barents Sea (red color in Fig. 2). The Atlantic Water that enters the Barents Sea densifies due to loss of heat and release of salt during sea ice formation. This dense shelf water flows into the Arctic interior through numerous submarine valleys with the St. Anna Trough (magenta in Fig. 2) being the most prominent.

The western branch of the NwAC and the remainder of the eastern NwAC branch continues towards the Fram Strait where a portion of AW turns south and recirculates in the Nordic Seas. The remainder enters the Arctic Ocean through the Fram Strait where the AW encounters the polar front of cold and fresh Arctic surface water, with the AW subducting into a sub-surface current (orange and green colors in Fig. 2) in the Eurasian basin. Observations show that the inflows of AW from the Nordic Seas to the Arctic Ocean through the Barents Sea and the Fram Strait are comparable in magnitude with a value of approximately 2 Sv (Rudels, 1987; Jones, 2001; Schauer et al., 2008). The Pacific water enters the Arctic Ocean through the shallow Bering Strait (≈0.8 Sv, Roach et al., 1995; Woodgate and Aagaard, 2005) and leaves the basin through the Fram Strait and the Canadian Archipelago (≈ −1.6 Sv, Curry et al., 2014).

4. Models descriptions

Fifteen models are used in the analysis, of which thirteen are described in the first CORE-II paper addressing the mean state of the North Atlantic (Danabasoglu et al., 2014). Most of the model details are given in that paper and are not repeated here. The models are listed in Table 1 together with the groups operating the models and the basic model information.

The analyzed models are based on three classes of vertical discretizations, the commonly used level or geopotential (z and z^*) coordinate models, isopycnic (σ) coordinate models, and hybrid coordinate models. In the Arctic Ocean, where air–sea–ice interactions, subduction of a boundary current, dense waters on the

Table 1
Summary of the participating models in alphabetical order. z refers to geopotential, vertical coordinate, z^* means z-star which is for rescaled geopotential coordinate, and σ_2 refers to isopycnic, vertical coordinate (the latter relative to a pressure at 2000 dbar).

Group	Ocean model	Horiz. res.	Grid	Vertical coordinate	Sea-ice model
AWI	FESOM 1.4	Nominal 1°	Bipolar	z	FESIM
BERGEN	NorESM-O	Nominal 1°	Tripolar	σ_2	CICE 4
CERFACS	NEMO3.2	Nominal 1°	Tripolar	z	LIM 2
CMCC	NEMO3.3	Nominal 1°	Tripolar	z	CMCC 4
CNRM	NEMO3.2	Nominal 1°	Tripolar	z	Gelato 5
FSU-HYCOM	HYCOM2.2.21	Nominal 1°	Bipolar	Hybrid	CSIM 5
FSU-HYCOMv2	HYCOM2.2.74	Nominal 0.72°	Tripolar	Hybrid	CICE 4
GFDL-GOLD	GOLD	Nominal 1°	Tripolar	σ_2	SIS1
GFDL-MOM	MOM4p1	Nominal 1°	Tripolar	z^*	SIS1
Kiel-ORCA05	NEMO3.1.1	Nominal 0.5°	Tripolar	z	LIM 2
MOM0.25	MOM5	Nominal 0.25°	Tripolar	z^*	SIS1
MRI-A	MRI.COM 3	1° × 0.5°	Tripolar	z	MK89; CICE
MRI-F	MRI.COM 3	1° × 0.5°	Tripolar	z	MK89; CICE
NCAR	POP 2	Nominal 1°	Bipolar	z	CICE 4
NOC	NEMO3.4	Nominal 1°	Tripolar	z	LIM 2

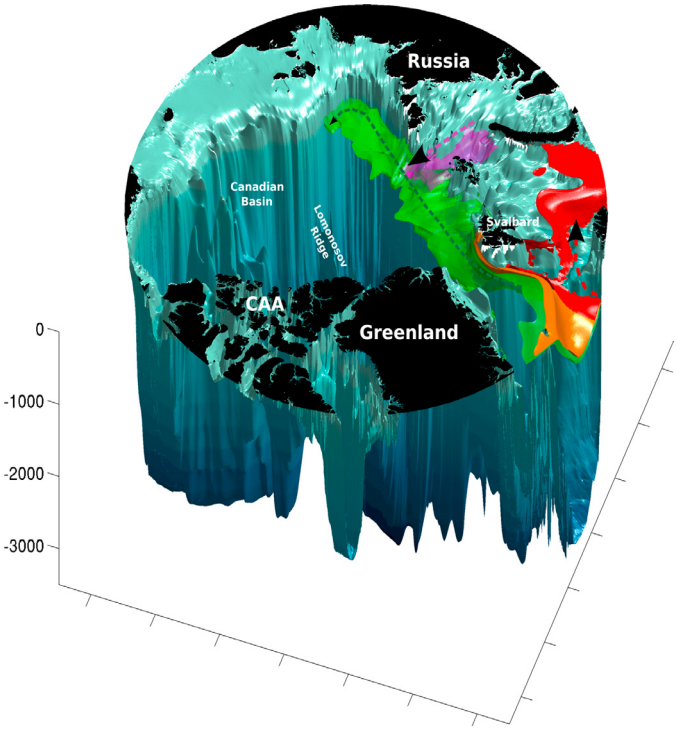

Fig. 2. Schematic of the main water masses of Atlantic origin in the Arctic Ocean using the PHC3.0 climatological data set. Red color represent water masses with a temperature of about 3 °C, representing flow of AW into the Barents Sea. Orange color represents the AW that subducts in or near the Fram Strait with a temperature of around 2.4 °C. Green color denotes the core of the Atlantic Inflow in the Eurasian Basin with a temperature of ≈1.4 °C. Magenta color is the cold deep water masses with a temperature of ≈ −1.5 °C, flowing down the St. Anna Trough. (For interpretation of the references to color in this figure legend, the reader is referred to the web version of this article.)

shelves and brine process are all crucial factors, the vertical representation and parameterization of these processes are also likely to be an important aspect in the simulated mean state.

The two models not included in Danabasoglu et al. (2014) are the global 0.25° MOM model and a newer version of HYCOM configured on a tripolar grid. The former is simply a finer resolution version of the 1 degree GFDL-MOM used in Danabasoglu et al. (2014). The higher resolution MOM might give us information about particular processes such as isopycnic mixing parameterization which is turned off in this model version. The new HYCOM ocean model employs a tripolar grid of finer resolution (0.72° vs. 1°) and it advects temperature and salinity rather than density and salinity compared to FSU-HYCOM.

As discussed by Griffies et al. (2009), ocean-ice models without a coupled, interactive atmosphere have to employ sea surface salinity restoring. The FSU-HYCOMv2 model coupled to CICE v4.0 employs a surface salinity restoring with a piston velocity of 50 m over 4 years everywhere except for the Antarctic region where the piston velocity is 50 m over 6 months.

The only unstructured-mesh model in the analysis is AWI-FESOM which is configured with a lateral resolution that is comparable to the majority of the other participating models. Seven different sea ice models are used in the 15 models. There are two models that modified their ocean physics specifically in the Arctic Ocean. These models are the BERGEN model where background diapycnic mixing is reduced to 10^{-6} m^2 s^{-1} and the Kiel-ORCA05 model where the salinity restoring is turned off under sea ice in the Arctic Ocean.

The analysis performed for the Arctic highlighted a bug in the CERFACS NEMO model. The NEMO grid is folded at the North Pole along a grid line extending from Canada to Asia at 78°W. On this specific grid line, the wind forcing fields need to be rotated in order to correspond to the local grid coordinates. This is not correctly done in the CERFACS simulation leading to spurious signals in ice dynamical fields. After having checked that the forcing error has a very local imprint and because the CERFACS results compare very well with all other diagnostics in the rest of the paper, we consider that it is still meaningful to keep CERFACS results in the current compilation.

All models except MRI-A are run for 300 years, corresponding to 5 repeated cycles of the 60-year forcing period following the CORE-II protocol (Griffies et al., 2012; Danabasoglu et al., 2014), covering the years from 1948 to 2007 (Large and Yeager, 2009). The ocean models are initialized with zero velocities and the January mean climatological temperature and salinity fields from the Polar Science Center Hydrographic Climatology (PHC3; a blending of the Levitus et al., 1998 data set with modifications in the Arctic Ocean based on Steele et al., 2001). The NCAR, FSU-HYCOM, Kiel-ORCA05, NOC, and FSU-HYCOMv2 models use, however, PHC2 rather than PHC3 for their initial hydrography.

The sea-ice models are initialized from sea ice states obtained from previous ocean sea ice coupled simulations (Danabasoglu et al., 2014). Typically, semi-equilibrium states are obtained after two model cycles in terms of both the Arctic Ocean sea ice state and the sea ice export fluxes (Q. Wang, personal communication).

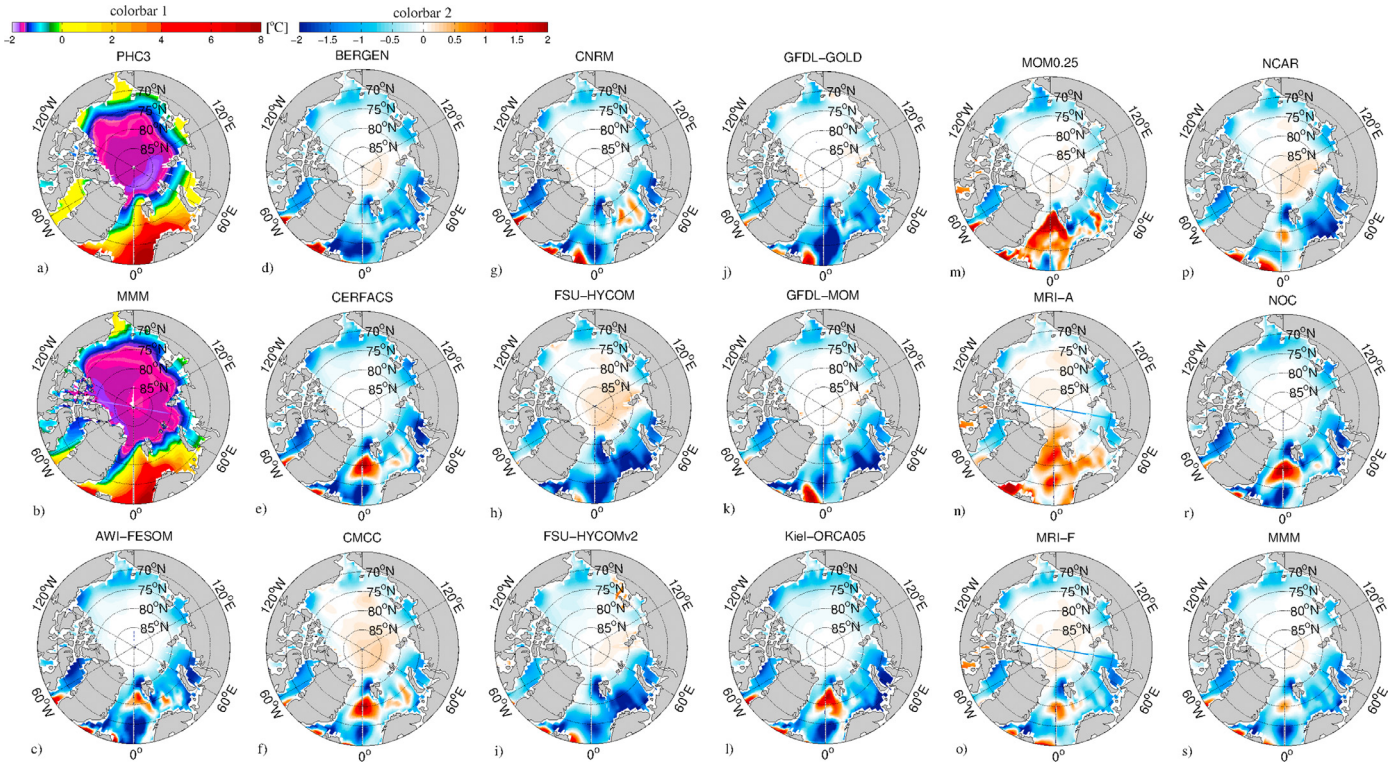

Fig. 3. (a) Map of the PHC3.0 climatology temperature field [°C] at $z = 5$ m. (b) MMM is the multi model mean of the temperature field, excluding the MRI-A model. (c–s) are maps of the time mean temperature field biases of different CORE-II models and MMM from PHC3.0. Colorbar 1 is for (a) and (b). Colorbar 2 is for (c–s).

The MRI-A assimilation model was run for 70 years starting from model year 231 of the MRI-F integration. The first 10 years are treated as spin-up and the remaining 60 years (associated with the period of CORE-II forcing) are used for the analysis.

Wang et al., 2016a; 2016b showed that most model simulations are equilibrated in the Arctic Ocean in terms of liquid fresh water content and total fresh water transport from the Arctic Ocean to the North Atlantic. All time mean results used in here are averaged over the last 30 years of the model simulations, corresponding to calendar years 1978–2007 of the fifth cycle. In this way, the inevitable adjustments in the simulated ocean properties during the first decades after the start of the model cycle in 1948 are small and likely negligible to the analyzed variations and patterns (He et al., 2016).

Although the presented model runs are forced by CORE-II, we do not advocate that CORE-II is better or worse than other available reanalysis products, neither on global scale or for the high, northern latitudes. There are some studies not published yet which compares different atmospheric datasets, but as of now the reliability of available reanalysis products is still an open research question (S. Yeager, personal communication).

5. Results

In this section, the basic features of the temperature and salinity fields and the associated biases are examined. Thereafter, time series of the heat and volume transports at the four gateways of the Arctic Ocean – the Bering Strait, the Davis Strait, the Fram Strait, and the Barents Sea Opening – are presented. The multi model mean (MMM) fields are computed from all but MRI-A, yielding a total of fourteen models. Because of the data assimilation used in MRI-A, discussions about this model is mainly presented in Section 5.4.

5.1. Arctic ocean temperature and salinity bias patterns

The PHC3.0 climatology and MMM of the temperature fields at 5 m depth are shown in Fig. 3(a) and (b), respectively. The most noticeable features are the warm AW entering the Eurasian Basin of the Arctic Ocean through inflow at the Fram Strait and the Barents Opening and likewise, but to a lesser degree, warm PW entering the Arctic Ocean through the Bering Strait, and the cold central Arctic Ocean.

Fig. 3(c)–(r) shows horizontal maps of time averaged temperature field biases relative to PHC3.0 at 5 m depth. Regular temperature fields are available in the supplementary material. Largest temperature biases are found near the periphery of the Arctic Ocean. All of the CORE-II models have a cold bias in the Chukchi Sea, and most of the models are anomalously cold in the Canadian Basin as well. Towards the Atlantic Ocean, AWI-FESOM, CERFACS, CMCC, Kiel-ORCA05, MRI-F, NCAR, MOM-0.25 and NOC share a dipole temperature pattern in the Fram Strait and south-west of Svalbard, with a warm bias at north and a cold bias at south. In addition to this feature, all but MOM-0.25 and MRI-A have cold biases in the Nordic Seas, and most of the models are cold in the Barents Sea as well.

Fig. 4 (c)–(f) provides horizontal maps of time averaged temperature biases at 400 m depth, which is close to the core of the warm AW in the Arctic interior. As a reference, the PHC3.0 climatology temperature field at 400 m depth is shown in Fig. 4(a) and the corresponding MMM is shown in Fig. 4(b).

The PHC3.0 climatological temperature shows warm AW entering the Arctic Ocean through the Fram Strait, the only peripheral opening at this depth (see FS in Fig. 1).The signature of the AW gradually diminishes along its eastbound trajectory in the Eurasian Basin (green outline in Fig. 1). On average, the temperature at this depth in the Canadian Basin (red outline in Fig. 1) is 1 °C below that in the Eurasian Basin. The St. Anna Trough region can be

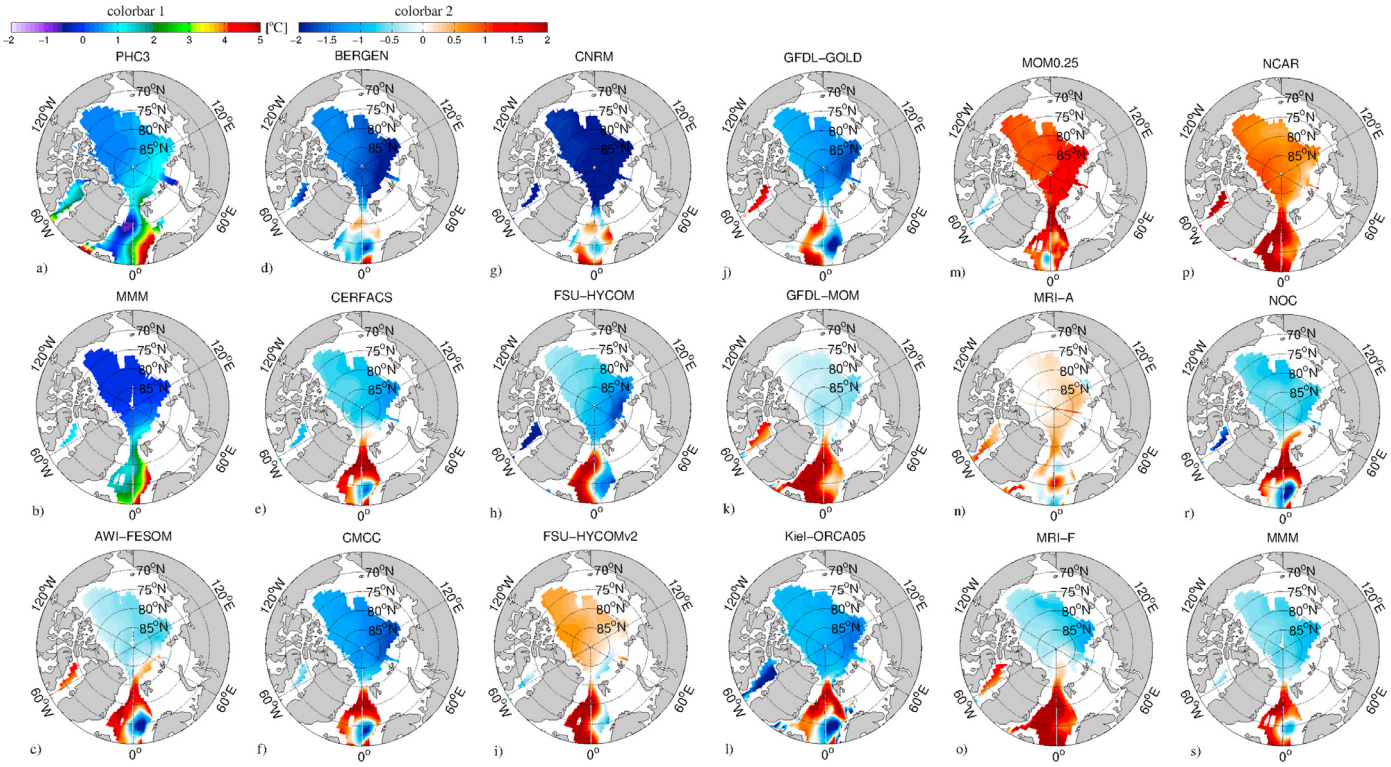

Fig. 4. The same as Fig. 3 but for $z = 400$ m.

identified from anomalously low-temperature waters. At this location cold and dense water masses from the shallow Barents and Kara Seas feed into the interior of the Arctic Ocean at intermediate depths (Jones, 2001; Rudels et al., 2013).

The multi model mean temperature field at 400 m (Fig. 4(b)) shows a wider and colder inflow of AW compared to PHC3.0. In addition, the AW signal disappears rapidly in MMM compared to that in PHC. There is also an overall cold bias in the Arctic interior in MMM. Only four of the models show basin-scale, positive temperature anomalies (MOM-0.25, MRI-A, NCAR and FSU-HYCOM).

As indicated by Fig. 4(p), the warm, basin-scale bias in NCAR is caused by the excessively warm AW in the Spitzbergen Current west of Svalbard (see below). NCAR has also insufficient amount of cold water entering the Arctic Ocean from the St. Anna Trough. A similar type of bias is also present in the coupled CESM simulations which use the same ocean model as in the NCAR contribution here (Danabasoglu et al., 2012).

The model closest to NCAR is the quarter degree MOM-0.25 model (Fig. 4(m)). MOM-0.25 has a pronounced warm anomaly in the the West Spitzbergen Current. MOM-0.25 shows indication of recirculation in the Fram Strait, likely caused by the higher resolution compared to the other models. The temperature anomaly at the outlet of the St. Anna Trough shows that this model has an outflow here, albeit of higher temperature than in climatology (see the original field in the supplementary material). An anomalously warm Nordic Seas is also seen in MRI-F. For the latter, the warm AW does only partly enter the Arctic Ocean.

The CNRM and CERFACS models are identical except for the horizontal eddy viscosity values (1×10^4 m^2 s^{-1} in CNRM and 2×10^4 m^2 s^{-1} in CERFACS) and the sea ice components; CERFACS uses LIM2 and CNRM uses Gelato5 (Danabasoglu et al., 2014). Despite the similarities, CNRM is considerably colder than CERFACS in the Arctic Ocean (Fig. 4(g) and (e)). The two models have also different temperature biases in the Nordic Seas, with CNRM close to but CERFACS warmer than PHC3.0. Dedicated numerical simulations are required to identify the underlying reasons for the differences in the simulated CNRM and CERFACS fields. Such a comparison is beyond the scope of this paper, but one can speculate that the different sea-ice models may influence the water mass transformation under and close to the sea-ice, whereas differences in the horizontal viscosity may influence the inflow of heat and salt into the Nordic Seas, including into the Barents Sea, and thus alter the water mass transformation formation rates on the shelves.

The two isopycnic coordinate ocean models BERGEN and GFDL-GOLD show prominent, cold biases in the Arctic Ocean, with largest deviations from climatology downstream of the St. Anna Through outflow (Fig. 4(d) and (j)). Examination of the evolution of the temperature field at 400 m depth in the different models (see the supplementary material) shows that all models with cold biases in the Central Arctic have excessive cold water spilling into the Arctic Ocean through the St. Anna Trough. Over time, the cold waters from the St. Anna Trough occupy the 400 m depth horizon in the Arctic interior. Other models which have a cold bias at 400 m are Kiel-ORCA05, FSU-HYCOM and CMCC. AWI-FESOM is arguably the model simulating the inflow of warm AW to the Arctic Ocean at this depth horizon closest to the observed climatology.

The PHC3.0 and MMM salinity fields at 5 m depth are shown in Fig. 5(a) and (b), respectively. The relatively salty inflow of PW is seen in the Bering Strait and in the shallow Chukchi Sea, whereas high-salinity waters of Atlantic origin are found in the Barents Sea, and in most of the Kara Sea and the Eurasian Basin. Low-salinity waters are clearly seen on the Eurasian shelves, mainly fed by river runoff. Within the applied contour interval, there is a fair agreement between the climatological and MMM salinity fields. But as for temperature, there are variations between the individual model realizations.

Fig. 5 (c)–(r) shows horizontal maps of time averaged salinity biases at 5 m depth for all of the models relative to PHC3.0. CERFACS, CNRM, FSU-HYCOM, FSU-HYCOMv2, Kiel-ORCA05, MRI-A, NCAR and NOC show all positive biases on the eastern shelves of

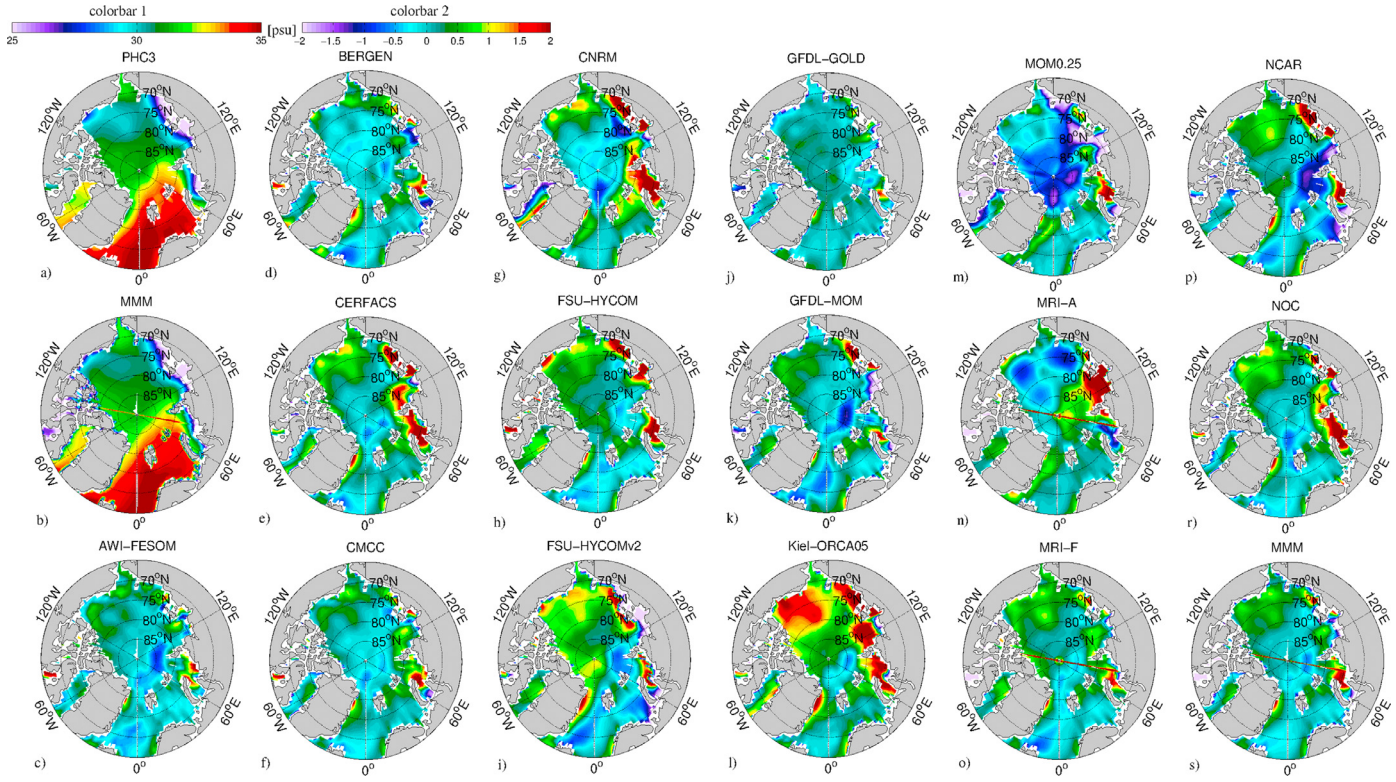

Fig. 5. Map of the PHC3.0 climatology salinity field [°C] at $z = 5$ m. (b) MMM is the multi model mean of the salinity field, excludingthe MRI-A model. (c–s) are maps of the time mean salinity field biases of different CORE-II models and MMM from PHC3.0. Colorbar 1 is for (a) and (b). Colorbar 2 is for (c–s).

the Arctic Ocean. All models but MOM-0.25 and MRI-A shows positive biases in the Canadian Basin. MRI-A, has a bias of 1–2 psu due to use of inadequate error statistics for assimilating coastal data, which is a problem specific to the data assimilation scheme.

Fig. 6 shows horizontal maps of time averaged salinity biases at 400 m depth. The PHC3.0 climatology field (Fig. 6(a)) shows a gradually disappearing high-salinity signature as the AW propagates into the Arctic interior. All models but MRI-A have a fresh bias in the Canadian Basin, with the MRI-F, GFDL-GOLD, CMCC, NOC and FSU-HYCOM showing the largest bias in this region. The NCAR, GFDL-MOM and MOM-0.25 models are comparable and close to the climatological value in the Eurasian Basin.

5.2. Vertical structure

Horizontally averaged temperature profiles for the Eurasian and the Canadian Basins are shown in Fig. 7(a) and (b), with the PHC3.0 climatology in dashed lines. A relatively warm core is evident in the PHC3.0 climatology between 200 and 400 m depth in the Eurasian Basin and 400–600 m depth in the Canadian Basin, representing the core of AW in the Arctic interior. The models can be grouped into three classes based on the character of the temperature biases in the Eurasian Basin (Fig. 7(a)): (i) those with warm biases below the core of AW (depth interval 500–2500 m), (ii) those with cold biases at the core depth of AW and also below 2500 m, and (iii) the remaining models with a cold bias at the depth of AW.

The models belonging to the warm group (i) are NCAR, GFDL-MOM, FSU-HYCOM, FSU-HYCOMv2, MRI-F, and MOM-0.25. These models are roughly 1 °C or more warmer than the observed temperature between 600 and 3000 m. The warm bias might be due to too warm AW and/or lack of dense water formation on the Barents/Kara/Siberian shelves and the subsequent spreading of these cold water masses. In addition, spurious vertical diffusion in geopotential coordinate models tends to give too strong vertical diffusion of heat in the Arctic Ocean (Griffies et al., 2000; Holloway et al., 2007; Ilıcak et al., 2012), an issue that should be assessed in detail but that has not been analyzed in the present study.

The cold biased models in group (ii) are CNRM, BERGEN, and GFDL-GOLD. These models suffer from relatively cold AW and excessive cold water exported through the St. Anna Trough. It is important to note that isopycnic models have to rely on explicitly prescribed vertical mixing parameterizations, since they have weak spurious numerical mixing (Ilıcak et al., 2012). Thus, lack of parameterized physics in the vertical mixing process and/or for the description of exchanges of water masses between the shelves and deep basins may be crucial factors in the BERGEN and the GFDL-GOLD simulations.

The interaction between the ocean and sea ice components and the effect of horizontal viscosity is another important factor to consider, exemplified by the excessive cold bias seen in CNRM but not in CERFACS, differing in the horizontal viscosity values and the choice of the sea ice model.

The third model group contains AWI-FESOM and the NEMO-based models Kiel-ORCA05, NOC, CMCC, and CERFACS. These models have all cold biases between 300 and 800 m in the Eurasia Basin. The cold bias extends deeper – to depths around 2000 m – in the Canadian Basin which receives heat from the Eurasian Basin. The latter might be due to either vertical mixing of the cold bias anomaly coming from the Eurasian Basin and/or simply too weak advection of heat from the Eurasian Basin. The intermediate resolution Kiel-ORCA05 model does not show any significant improvement in comparison with the other NEMO-based models, likely because the core of AW is not well simulated in this model group, see Fig. 4.

The AWI-FESOM model has overall the most realistic vertical structure albeit with a slightly too cold and too deep core of AW and some warm biases between 500 and 2000 m.

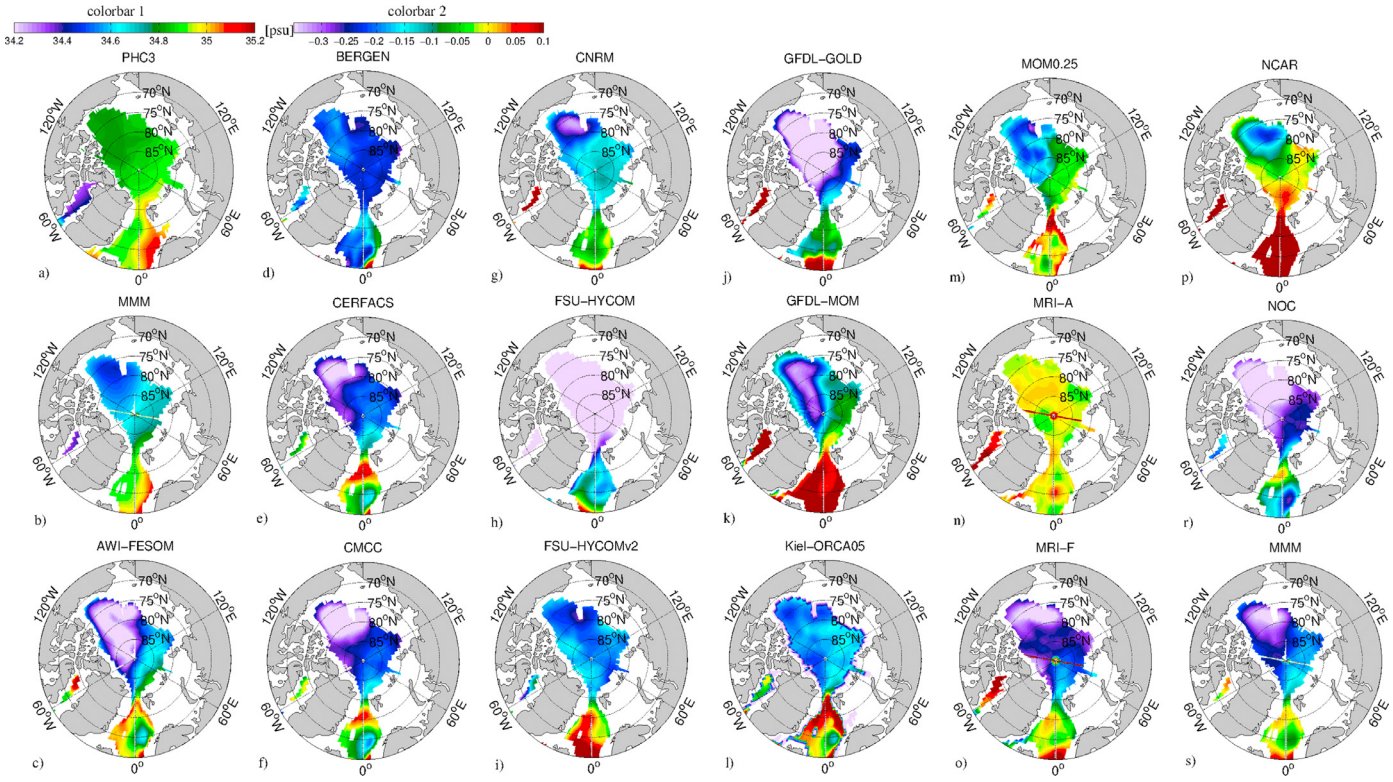

Fig. 6. The same as Fig. 3 but for $z = 400$ m.

Fig. 7 (c) and (d) displays horizontally averaged salinity bias profiles in the Eurasian and Canadian Basins. In the Eurasian basin below 50 m, all models but MRI-A and NOC are fresher than the observed climatology. The NCAR model has a positive salinity anomaly between 350 m and 2000 m, which is probably due to the Atlantic inflow since the NCAR has a pronounced AW signature at similar depths.

For the rest of the models, there is a strong negative bias between 50 m and 400 m (approximately at the core depth of AW). One possible reason for the negative salinity bias in the upper ocean is the parameterization of brine formation and the descent of high-salinity water masses into the interior of the Arctic Ocean, coupled to transport and mixing process. Most of the current parameterizations put salt that is released during sea ice formation at the surface rather than distributing it in the water column. Nguyen et al. (2009) found that this approach leads to excessive vertical mixing, and that it may destroy the steep salinity gradient associated with the halocline. In the Canadian Basin, all models have positive biases in the upper 75 m. Likewise, all CORE-II models except MRI-A and NCAR, have negative biases below 500 m.

The above findings indicate that weak (strong) inflow of AW and strong (weak) water mass conversion in the Barents and Kara Seas are the main factors for large-scale negative (positive) temperature (and possibly salinity) biases in the Arctic Ocean. To further elaborate on this, the vertical distribution of observed and simulated temperature, extending from the Kara Sea via the St. Anna Trough and across the North Pole to the Canadian Archipelago (from 70°E to 110°W; see Section S1 in Fig. 1), is presented in Fig. 8.

In the PHC3.0 climatology (Fig. 8(a)), the warm AW is mainly confined to the depth range 200–1000 m in the interior of the basin. Above the warm AW, a cold and shallow halocline (not shown) at 150–200 m depth is evident across the Arctic Ocean. The cold water in the St. Anna Trough (rightmost arrow in Fig. 8(a)) partly feeds the upper halocline and partly sinks and ventilates the deeper portions of the Arctic basin.

In NCAR, AW is much more extensive and much warmer than in the PHC3.0 climatology (Fig. 8(o)). In this case, absence of cold water transformation in the Barents/Kara Seas is clearly visible at the position of the St. Anna Trough, with a simulated temperature 2 °C higher than in the observations. The GFDL-MOM model has much deeper AW than in the observations (Fig. 8(j)), but with some cold water on the eastern portion of the Kara shelf. The free run of the MRI model suffers from a warm bias below 600 m in the Arctic interior (Fig. 8(n)) in a manner comparable to that in GFDL-MOM.

The NEMO-based models perform similarly except for the CNRM model, the latter showing hardly any AW at all. The NOC and AWI-FESOM models are both favorable in terms of position and amplitude of the AW. There is a strong warm anomaly throughout the Arctic Ocean in the other warm bias FSU-HYCOM, FSU-HYCOMv2, and MOM-0.25 models (Fig. 8(g), (h) and (l)). In the former, heat penetrates all the way to the deepest portions of the Eurasian Basin. The BERGEN and GFDL-GOLD models have somewhat realistic vertical structures in the deep interior of the basin, but with a far too weak core of the AW. Cold, dense water sinks and accumulates in the Eurasian abyss (below 4000 m) in the GFDL-GOLD model.

Vertical sections of temperature along the main path of the Atlantic Inflow, see section S2 in Fig. 1, are presented in Fig. 9. Observed temperature shows a gradual cooling of the inflowing AW, and that the AW subducts below the upper (fresh) surface water just north of the Fram Strait (the leftmost arrow in Fig. 9(a)). Intrusions of two low-temperature water masses are seen north of the Fram Strait. The location of the first deep ($>$ 1500 m), cold water mass intrusion is found east of the Yermak Plateau (at about $x = 1700$ km), whereas the second intrusion is at the exit of the St. Anna Trough ($x = 2450$ km, at the rightmost arrow in Fig. 9(a)).

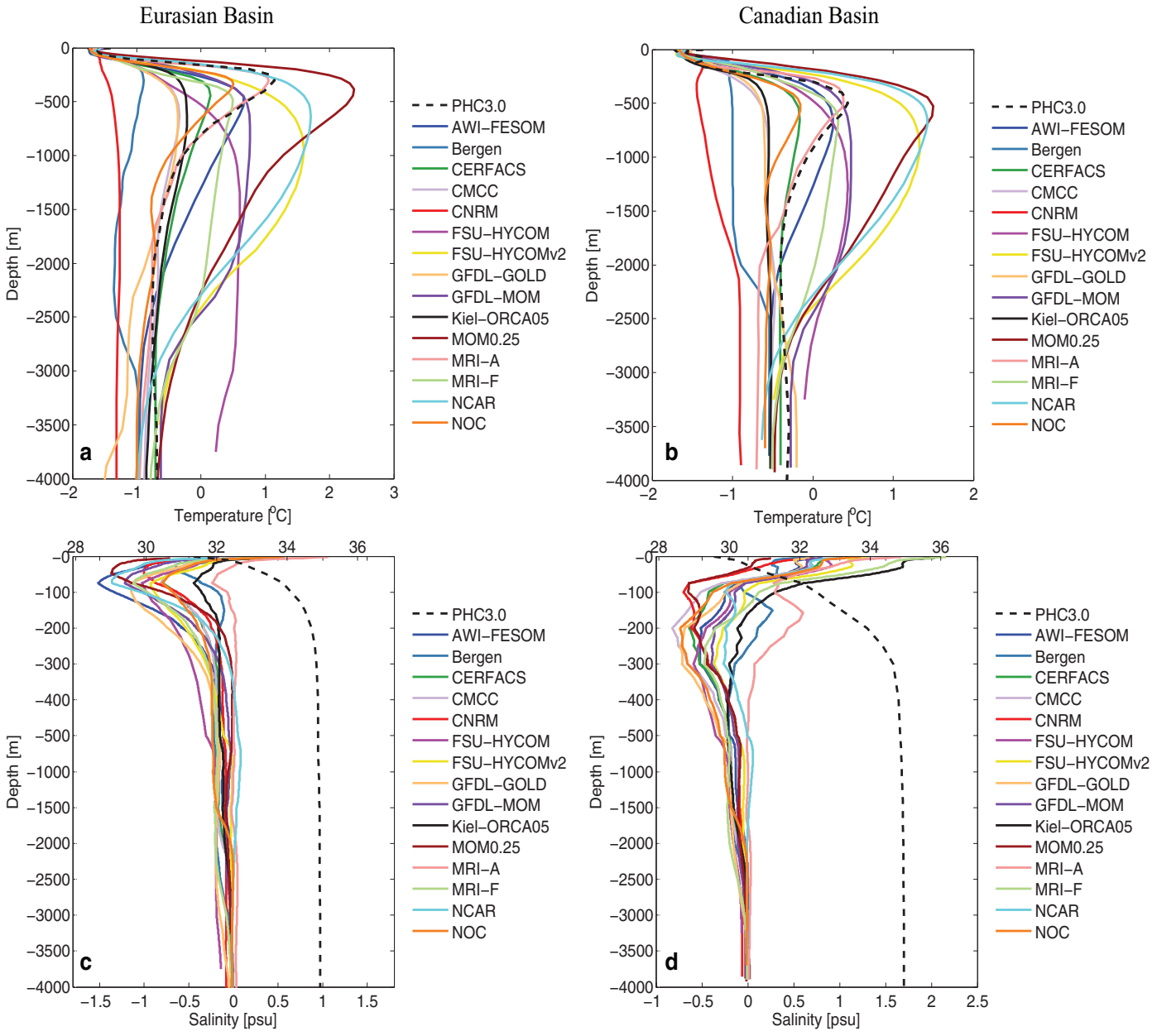

Fig. 7. Horizontally averaged vertical temperature profiles in the (a) Eurasian Basin and (b) the Canadian Basin. Horizontally averaged vertical salinity bias profiles in the (c) Eurasian Basin and (d) the Canadian Basin. The scales of mean salinity field of PHC3.0 (dashed lines) are at the top of (c) and (d). The biases are computed by subtracting PHC3.0 salinity profile from the model data and the scales of anomalies are shown at the bottom of the figures. Note that vertical axis is stretched in the upper 500 m in (c) and (d).

For the majority of models, AW subducts just before or at the Fram Strait (close to $x = 1200$ km). Exceptions are the MRI-A and MOM-0.25 models, where subduction occurs just north of the Fram Strait ($x \approx 1500$ km). The subduction phenomena is linked to many processes (Price, 2001) that need to be parameterized in the rather coarse resolution models taking part in this study. Accurate modeling of the subduction processes would likely require higher resolution models with a realistic representation of the varying thickness of the seasonal mixed layer depth, eddy mixing along local neutral surfaces, eddy restratification of density fronts (Gent and McWilliams, 1990; Marshall, 1997), and eddy-topography interactions (Holloway et al., 2007).

A prominent feature in most models is an Atlantic layer extending too deep compared to the PHC3.0 climatology at the Fram Strait. This feature is particular evident in the NCAR, GFDL-MOM, FSU-HYCOM and FSU-HYCOMv2 models. Cold sub-surface waters originating from the St. Anna Trough are visible in the two isopycnic models BERGEN and GFDL-GOLD (at about $x = 2500$ km), and possibly in CNRM above 1000 m and in NOC at a depth of about 1500 m. In CERFACS, GFDL-MOM, AWI-FESOM, MRI-F, Kiel-ORCA05, CMCC and FSU-HYCOM the temperature signal of the AW is substantially weakened after the St. Anna Trough. It could be that cold shelf water is indeed blending with the AW in these models but in a more vertically homogeneous manner than BERGEN, GFDL-GOLD, CNRM and NOC.

5.3. March mixed layer depths

Fig. 10 displays the mean March climatological mixed layer depths (MLD) of the Monthly Isopycnal and Mixed-layer Ocean Climatology (MIMOC) product and of the different CORE-II models. The depth of the surface mixed layer is a particularly crucial

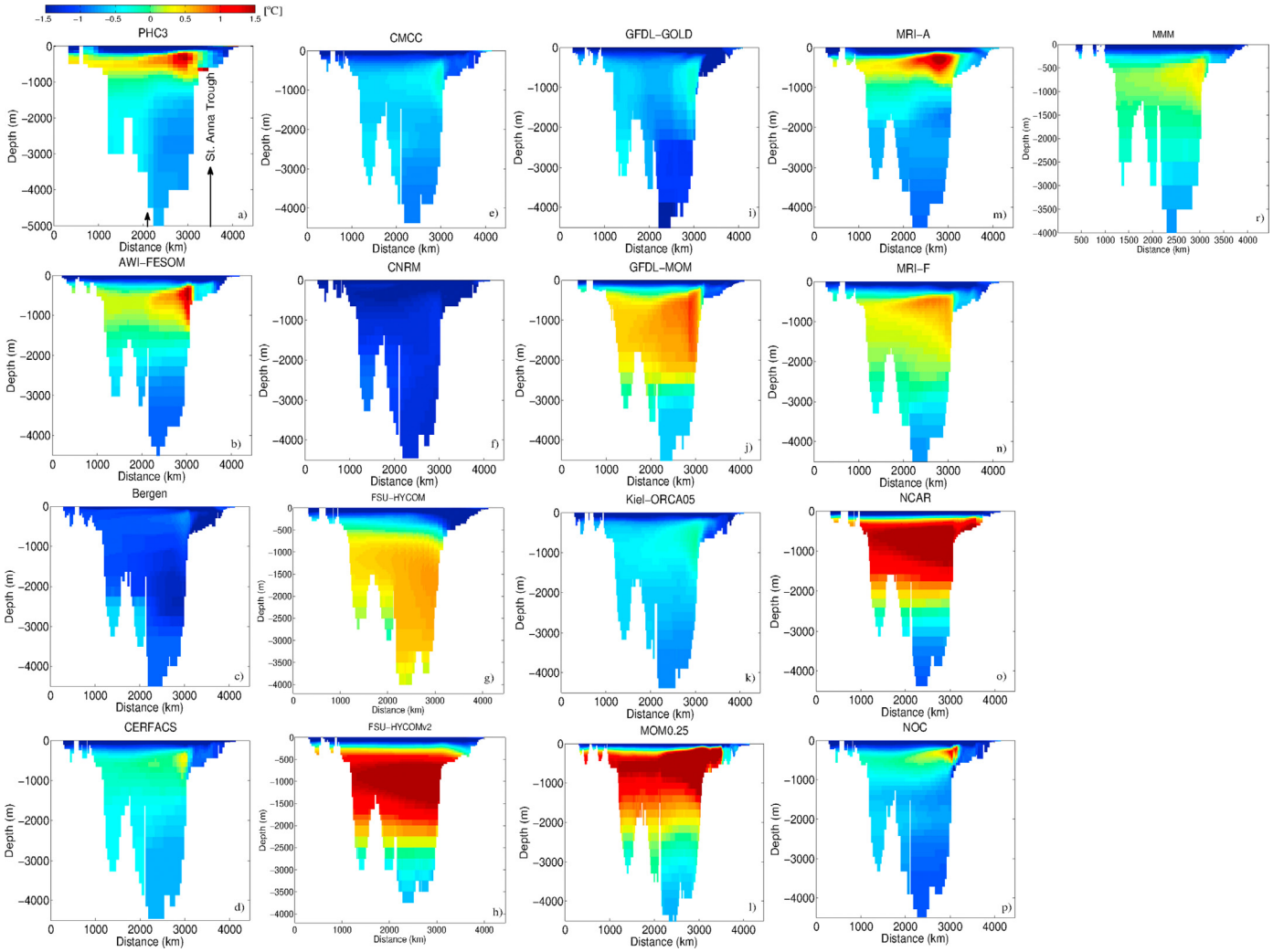

Fig. 8. Vertical section of the mean temperature field [°C] between 70°E and 110°W along S1 for (a) PHC3.0 and (b–r) different CORE-II models and MMM. Starting point of S1 is at lon = 110°W and lat = 70°N. The left arrow in (a) is the location of the North Pole while the right arrow shows the St. Anna Trough.

component in the Arctic Ocean for physical, chemical and biological processes (Peralta-Ferriz and Woodgate, 2014). Transfer of heat and fresh water/salt across the air-ice-sea interface can be significantly affected by MLDs. The MIMOC field is used instead of PHC3.0 since the former includes the latest Ice-Tethered Profilers (Schmidtko et al., 2013). Recently, Timmermans et al. (2012) used Ice-tethered profiler (ITP) measurements and computed the mixed layer depths only in the Canadian Basin. Peralta-Ferriz and Woodgate (2014) employed all available observational data except ITP data to compute winter and summer MLDs in Arctic basins. They showed that maximum MLD in winter is found in the Barents Sea with values about 110 m. The MLD in the Eurasian Basin is second deepest, while that in the Makarov Basin is the third deepest (about 50 m). In the following, the MLD is set to the depth where the density difference between the surface density and the sub-surface potential density (referenced to the surface) exceeds 0.125 kg m^{-3}. This definition is similar to that suggested by Timmermans et al. (2012). For the CORE-II models, we use 30 years of March (1978–2007) mean temperature and salinity fields from the last cycle to compute the MLD field.

The interior of the Arctic Ocean has an observation-based MLD of approximately 30 m (Fig. 10(a)). There are two strong convection regions in March in the climatology; (i) south of Svalbard with MLDs in excess of 400 m, and (ii) in the Barents Sea the MLD extends essentially throughout the water column (around 300 m). Maximum MLD in MIMOC is at the west of 0° longitude and close to the ice-edge, west of Greenland. However, maximum MLD in MMM is at the east side of 0° longitude (Fig. 10(b)). This difference might be caused by an erroneously located sea-ice edge in the models. All models except AWI-FESOM show deep MLDs south Svalbard. Deep convection in this region coincides with excessive loss of heat in the models. The excessive convection is likely related with improper physics in the models as mentioned in the previous section.

5.4. Data assimilated MRI results

The data assimilated results provided by MRI-A is in closest agreement with the climatological temperature field at 400 m depth (Fig. 4(n)). In this case, MRI-A captures the intrusion of the Atlantic inflow and has a reasonable representation of the Nordic Sea water properties. In addition, MRI-A is also in close agreement with the observed temperature distribution at the Atlantic inflow and the Arctic Ocean sections (Figs. 9(m) and 8(m)). For the salinity field, the MRI-A model follows the PHC3.0 climatology in the deep ocean, but with approximately 1 psu bias at the surface in both the Eurasian and the Canadian Basins.

Overall MRI-A is, as expected based on the data assimilation scheme, the model closest to the observed temperature field. The short integration time (60 years) may contribute to this. Analysis

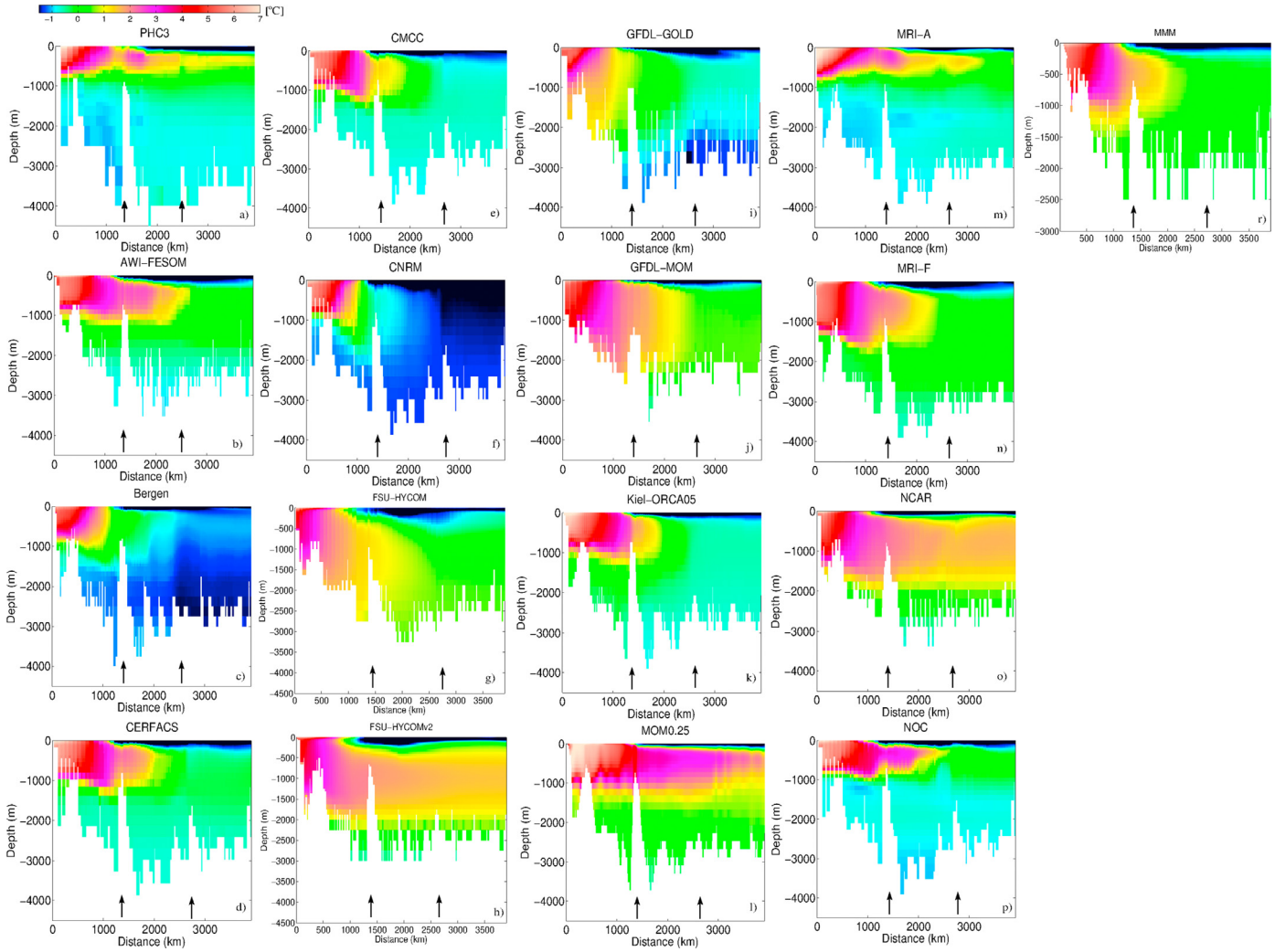

Fig. 9. Vertical section of the mean temperature field [°C] at Section 2 in Fig. 1 for (a) PHC3.0, (b–r) the different CORE-II models and MMM. Starting point of S2 is at lon = 17.5°E and lat = 69°N. The left arrow in all panels is the location of the Fram Strait while the right arrow shows the St. Anna Trough.

indicates that biases tend to develop over time as seen from 300 years simulations with the other models (see the supplementary movies).

5.5. Heat and volume transports at the Arctic Ocean gateways

The Arctic Ocean receives water of Atlantic origin in the Fram Strait and across the Barents Opening, and water of Pacific origin in the Bering Strait. The outflow of water from the Arctic Ocean takes place through the Fram Strait and the Canadian Archipelago. Transport values vary dependent on the time period and the actual analysis of the available observations. The mass budget is not necessarily closed for the Arctic Ocean due to uncertainties in the measurements as well as temporal variations (Bezczynska-Möller et al., 2011), and Curry et al. (2011) found that heat transport values may differ if the mass transport is not properly closed.

The following numbers are commonly cited for the mass transports: an inflow of about 2.0 Sv through the Barents Opening (based on measurements between 1997 and 2007, from Smedsrud et al., 2013; Skagseth et al., 2008), and an inflow through the Bering Strait of 0.8 ± 0.2 Sv (1990–2007, from Roach et al., 1995; Woodgate and Aagaard, 2005). These two inputs are balanced by a net outflow through the Fram Strait of 2.3 ± 4.3 Sv (1997–2007, from Schauer et al., 2008; Curry et al., 2011) and through the Davis Strait of 1.6 ± 0.2 Sv (2004–2010, see Curry et al., 2014).

In the following we discuss the mean volume and heat transports and their temporal variations at the Arctic Ocean gateways. The volume and heat transports are divided into two parts with the convention that *positive* values imply flow into the Arctic Ocean and *negative* values imply outflow from the Arctic Ocean. For the heat transport values, 0 °C is used as the reference temperature.

5.5.1. Bering Strait

Table 2 shows the mean and standard deviation of volume and heat transports of the CORE-II models at the Bering Strait. All models simulate transport into the Arctic Ocean (i.e., positive transport values). The multi-model mean volume transport (excluding MRI-A) is 0.99 Sv. Observational estimates indicate a flow of 0.8 ± 0.2 Sv (Roach et al., 1995; Woodgate and Aagaard, 2005). The GFDL-GOLD model has the weakest transport with 0.25 Sv, whereas MRI-A, MRI-F and Kiel-ORCA05 have the strongest transports with 1.31 Sv. The multi model mean heat transport at the Bering Strait is 3.39 TW, with the weakest heat transports found in FSU-HYCOM and GFDL-GOLD. In addition, the standard deviation of the heat transport in GFDL-GOLD is much smaller than for the other CORE-II models.

Fig. 11 displays the temporal anomalies of the simulated heat and volume transports. All of the models show similar variations, although the magnitude of the deviations differ, with GFDL-GOLD

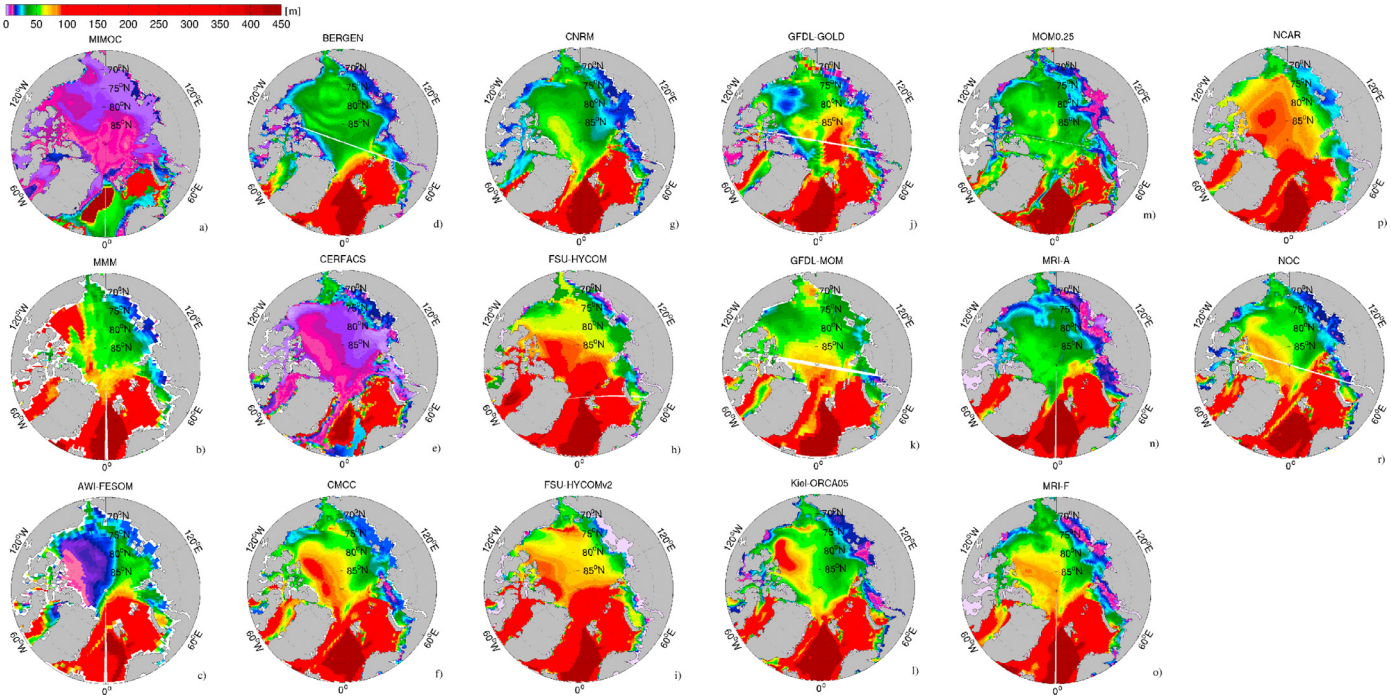

Fig. 10. March mean mixed layer depth [m] computed from (a) the MIMOC climatology field and (b–r) last 30 years March mean of the different CORE-II models.

Table 2
The mean Bering Strait net volume and heat transports and the standard deviation of the annual mean time series. Positive values indicate flux into the Arctic Ocean. The last 60 model years (1948–2007) are used in the analysis. MMM is the multi model mean.

Model	Mean volume transport [Sv]	Standard deviation [Sv]	Mean heat transport [TW]	Standard deviation [TW]
Observed	0.8 ± 0.2	0.6 to 1		
AWI-FESOM	1.05	0.09	3.49	1.85
Bergen	0.83	0.05	3.34	1.23
CERFACS	1.18	0.13	4.13	2.06
CMCC	1.18	0.13	2.82	1.9
CNRM	1.21	0.16	4.71	2.2
FSU-HYCOM	1.01	0.12	0.83	1.6
FSU-HYCOMv2	0.85	0.07	2.89	1.47
GFDL-GOLD	0.25	0.02	1.16	0.4
GFDL-MOM	0.66	0.06	3.86	1.23
Kiel-ORCA05	1.31	0.14	5.48	2.51
MOM0.25	1.17	0.11	2.41	1.69
MRI-A	1.31	0.13	5.08	1.99
MRI-F	1.31	0.12	4.93	2.05
NCAR	0.76	0.08	3.56	1.41
NOC	1.19	0.13	3.88	1.96
MMM	0.99	0.09	3.39	1.49

showing the smallest amplitudes. Year-to-year variations are most prominent, with very weak decadal-scale variations. The flow across the Bering Strait and CAA is largely controlled by the sea surface height gradient across the gateways (Peterson et al., 2012; McGeehan and Maslowski, 2012). The common atmospheric state, influencing the dynamic and thermosteric ocean states in similar manners, are likely the reason for the similarity across the models.

5.5.2. Davis Strait

The mean and standard deviation of volume and heat transports at the Davis Strait are given in Table 3. As expected, all models show volume transport out of the Arctic Ocean at this location. The multi model mean volume transport is −1.75 Sv. Cuny et al. (2005) estimated a volume transport of -2.6 ± 1.0 Sv through Davis Strait between 1987 and 1990, while Curry et al. (2014) estimated a transport of -1.6 ± 0.2 Sv between 2004 and 2010. The weakest and strongest volume transports are found in GFDL-MOM and the high resolution MOM-0.25, respectively. The multi model mean heat transport at the Davis Strait is 13.44 TW which is lower than the observational estimates of 18 ± 17 TW by Cuny et al. (2005) and 20 ± 9 TW by Curry et al. (2011).

The temporal variations in the heat and volume transports across the Davis Strait are shown in Fig. 12. In contrast to the Bering Strait transport, there is a strong decadal-scale signal in the volume transport with increasing values from the 1950s to the 1970s and decreasing values towards the end of the 1980s. All models show an increase in the volume transports since the early 1990s. In contrast, there is no clear signal in the heat transport emerging from the model simulations. Lack of decadal signal in the heat transport time series is caused by a compensating change in temperature (relative to 0 °C) and the volume transport.

5.5.3. Barents Sea opening

Based on available observations, Skagseth et al. (2008) estimate that the mean net volume and heat fluxes through the BSO during 1998–2006 were 1.8 Sv and 48 TW, respectively.

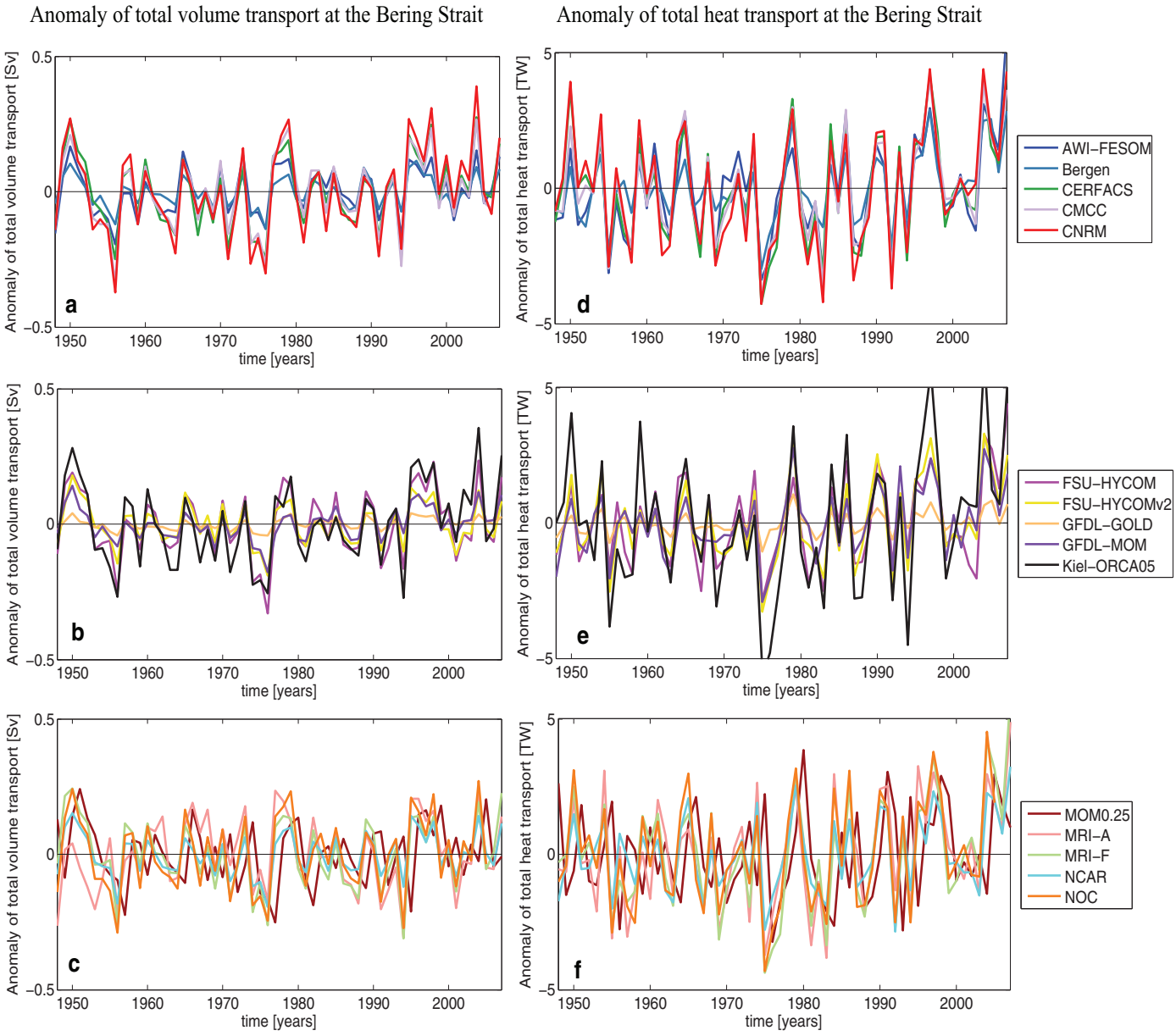

Fig. 11. Left: Anomaly of annual volume transport across the Bering Strait, unit is Sv. Right: Anomaly of annual heat transport across the Bering Strait, unit is TW.

Table 3
The mean Davis Strait net volume and heat transports and the standard deviation of the annual mean time series. Negative values indicate flux out of the Arctic Ocean. The last 60 model years (1948–2007) are used in the analysis. MMM is the multi model mean.

Model	Mean volume transport [Sv]	Standard deviation [Sv]	Mean heat transport [TW]	Standard deviation [TW]
Observed	−2.6 ± 1.0 to −1.6 ± 0.2	0.3	20 ± 9 to 18 ± 17	
AWI-FESOM	−1.13	0.19	14.64	4.28
Bergen	−1.80	0.29	10.178	1.73
CERFACS	−2.45	0.46	13.91	2.51
CMCC	−2.19	0.43	14.65	2.28
CNRM	−2.64	0.48	20.37	3.06
FSU-HYCOM	−0.53	0.1	6.09	1.12
FSU-HYCOMv2	−2.07	0.25	19.71	1.7
GFDL-GOLD	−1.23	0.18	11.09	1.41
GFDL-MOM	−0.51	0.09	11.09	1.47
Kiel-ORCA05	−2.33	0.45	14.18	4.46
MOM0.25	−3.12	0.69	17.05	3.36
MRI-A	−0.93	0.34	3.72	2.99
MRI-F	−0.70	0.26	8.73	2.75
NCAR	−1.53	0.14	13.44	1.43
NOC	−2.18	0.43	13.1	2.26
MMM	−1.75	0.27	13.44	1.39

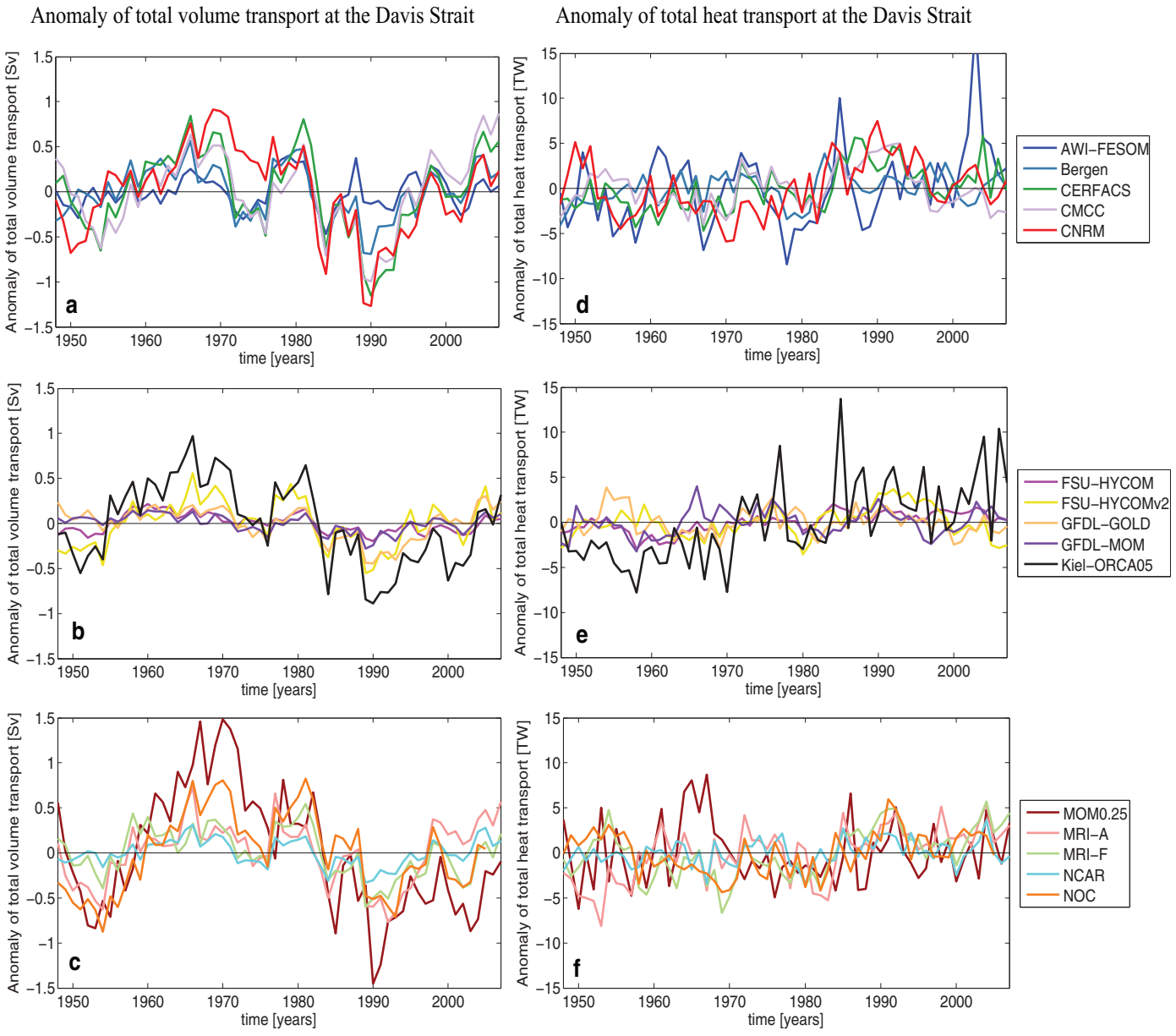

Fig. 12. Left: Anomaly of annual volume transport across the Davis Strait, unit is Sv. Right: Anomaly of annual heat transport across the Davis Strait, unit is TW.

Furthermore, the observation-based estimates indicate that the volume (heat) transport dropped from ≈2 Sv (≈50 TW) to ≈1 Sv (≈30 TW) between 1998 and 2001. Thereafter both volume and heat transports increased to 3 Sv and 60 TW, respectively, in 2003. Similar variations in the fluxes (a decrease followed by an increase) were observed in 2003 and 2006. Skagseth et al. (2008) conclude that there has been a slight increase in the ocean heat transport into the Arctic Ocean through the Barents Sea since 1998.

Mean volume and heat transports from the CORE-II models at BSO are given in Table 4. There are large differences in the magnitude of heat and volume transports across the models. All models simulate a net eastward (into the Barents Sea) volume transport, with the MMM volume transport across the BSO being 2.53 Sv. The CNRM (FSU-HYCOMv2) model has the strongest (weakest) volume flux through BSO, mirroring the results from the Fram Strait since the net eastward flow is mainly a compensation for the net southward flow through the Fram Strait (see Section 5.5.4). All models have high negative correlations between the volume fluxes at BSO and at the Fram Strait (see Fig. 15; 10 out of 15 models have correlations $r > 0.8$, with the smallest and the largest value 0.64 and 0.91, respectively). Observations suggest a similar relationship (Rudels et al., 1994).

Yearly anomalies of volume and heat transports through BSO are shown in Fig. 13. Although the mean volume transports differ between the models, they all capture similar interannual to decadal variations, including similarities with the observed variations between 1998 and 2006. This holds for both the volume and heat transports. There is an increasing volume flux in some models (e.g., NCAR, GFDL-MOM, MRI-F, BERGEN, NOC) between 1970 and 2007. The heat transport through the Barents Sea roughly doubles its value in these models. Despite model differences in the east- and westward heat transports across the BSO (not shown here), all models simulate a net increase in the transport during the last two decades. Some models (NCAR, FSU-HYCOM, FSU-HYCOMv2) have weaker heat transports at BSO, possibly because of a weaker volume transport. The multi model mean heat transport across the BSO is 53.96 TW.

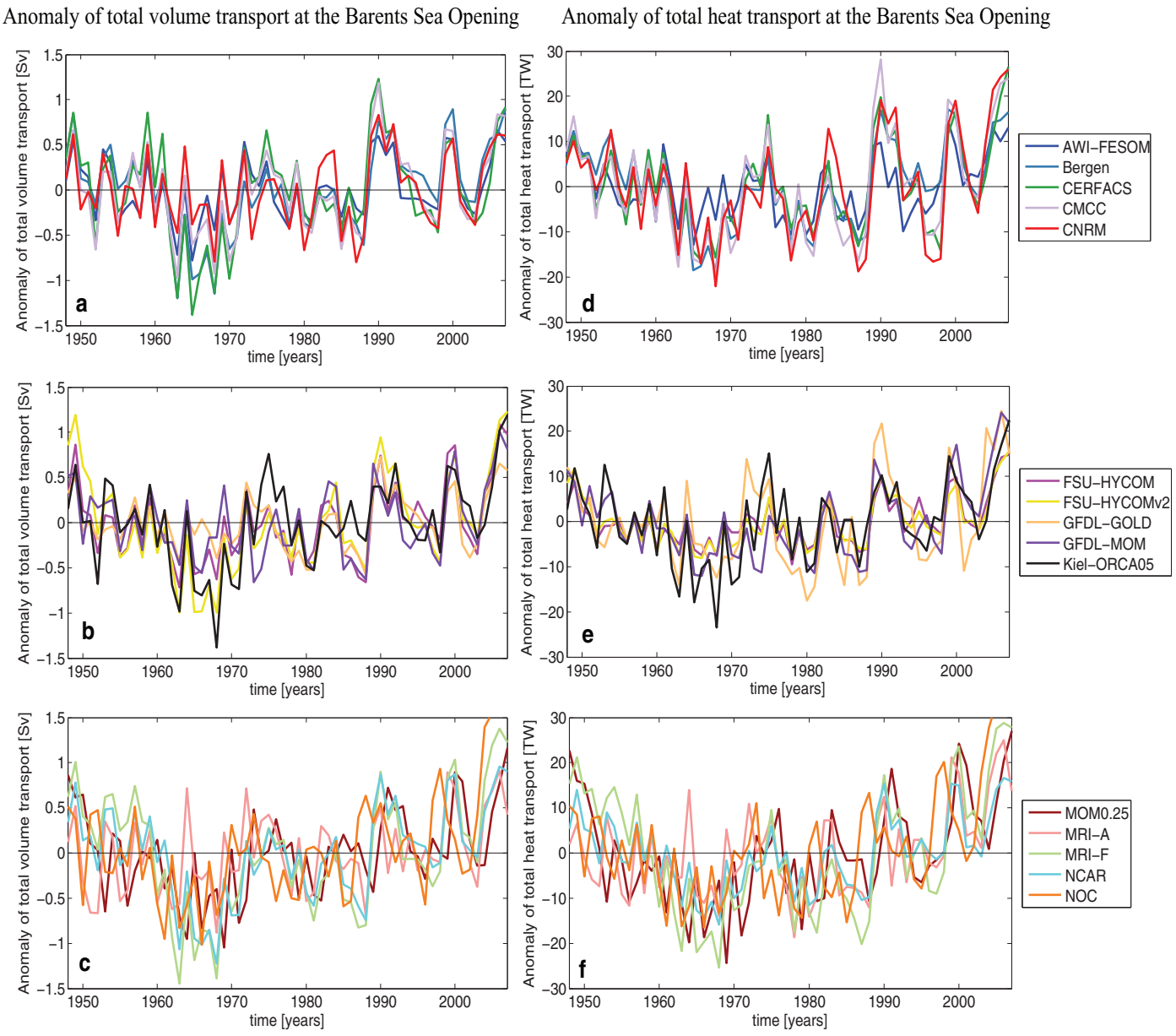

Fig. 13. Left: Anomaly of annual volume transport across the Barents Sea Opening, unit is Sv. Right: Anomaly of annual heat transport across the Barents Sea Opening, unit is TW.

5.5.4. Fram Strait

Observation-based estimates by Schauer et al. (2008) and Bezczynska-Möller et al. (2011) between 1997 and 2006 indicate a net southward transport of about 2 Sv, consisting of a southward transport across the Fram Strait of about 5–7 Sv and a northward flow of about 3–5 Sv. Variations in the inflow, outflow and, notably, recirculation within the strait, together with difficulties observing the flow towards the sea-ice covered region off Greenland, puts large uncertainties to these values (Bezczynska-Möller et al., 2011).

The mean Fram Strait volume and heat transports are provided in Table 5. The multi-model mean volume transport (excluding MRI-A) is 1.95 Sv, directed out of the Arctic Ocean. FSU-HYCOMv2 is the only model with a net northward volume transport (0.23 Sv) through the Fram Strait. The NCAR, BERGEN and MOM-0.25 models have relatively weak total volume transports of about −1 Sv. Mean total transport in NOC, GFDL-GOLD, CERFACS, and AWI-FESOM is around −2 Sv, and is thus in agreement with the observed, net transport. However, all models underestimate the observation-based northward and southward directional transports, typically by a factor of two or more (not shown). Barrier et al. (2015) described that the Fram Strait transport can be suppressed if North Atlantic Current is too zonal, leading to anomalously large volume and heat transports between the Faroes and Scotland, but less total transport into the Nordic Seas.

As mentioned, the transport values computed here might depend on the actual location of the section S1 (Fieg et al., 2010; Jahn et al., 2012; Bezczynska-Möller et al., 2011) in comparison to the amount and location of recirculation of the water masses in the Fram Strait in the models.

Yearly averaged time series of the anomalous volume transports in the Fram Strait are shown in Fig. 14. Despite the common CORE-II forcing protocol, the turbulent fluxes, computed by bulk formulae, strongly depend on the simulated ocean and sea-ice states. Because of differences in these states, in addition to resolution and mixing dependent recirculation issues in the Fram Strait,

Table 4
The mean Barents Sea Opening net volume and heat transports and the standard deviation of the annual mean time series. Positive values indicate flux into the Barents Sea. The last 60 model years (1948–2007) are used in the analysis. The observed values are based on transports provided by Smedsrud et al. (2013). MMM is the multi model mean.

Model	Mean volume transport [Sv]	Standard deviation [Sv]	Mean heat transport [TW]	Standard deviation [TW]
Observed	2–2.3	0.8 to 2.9	70 ± 5	
AWI-FESOM	2.3	0.34	60.65	7.17
Bergen	2.32	0.49	51.48	9.61
CERFACS	3.26	0.57	43.6	10.39
CMCC	3.71	0.49	76.4	12.17
CNRM	4.55	0.42	54.07	12.05
FSU-HYCOM	1.49	0.43	20.07	5.6
FSU-HYCOMv2	0.88	0.52	18.61	5.65
GFDL-GOLD	2.81	0.32	68.54	10.86
GFDL-MOM	1.89	0.42	40.84	8.93
Kiel-ORCA05	2.21	0.51	56.94	9.43
MOM0.25	2.98	0.48	83.66	11.64
MRI-A	2.52	0.42	64.1	10.15
MRI-F	2.99	0.65	63.58	13.65
NCAR	1.46	0.54	35.86	8.43
NOC	2.73	0.61	64.42	13.07
MMM	2.53	1.06	53.96	21.15

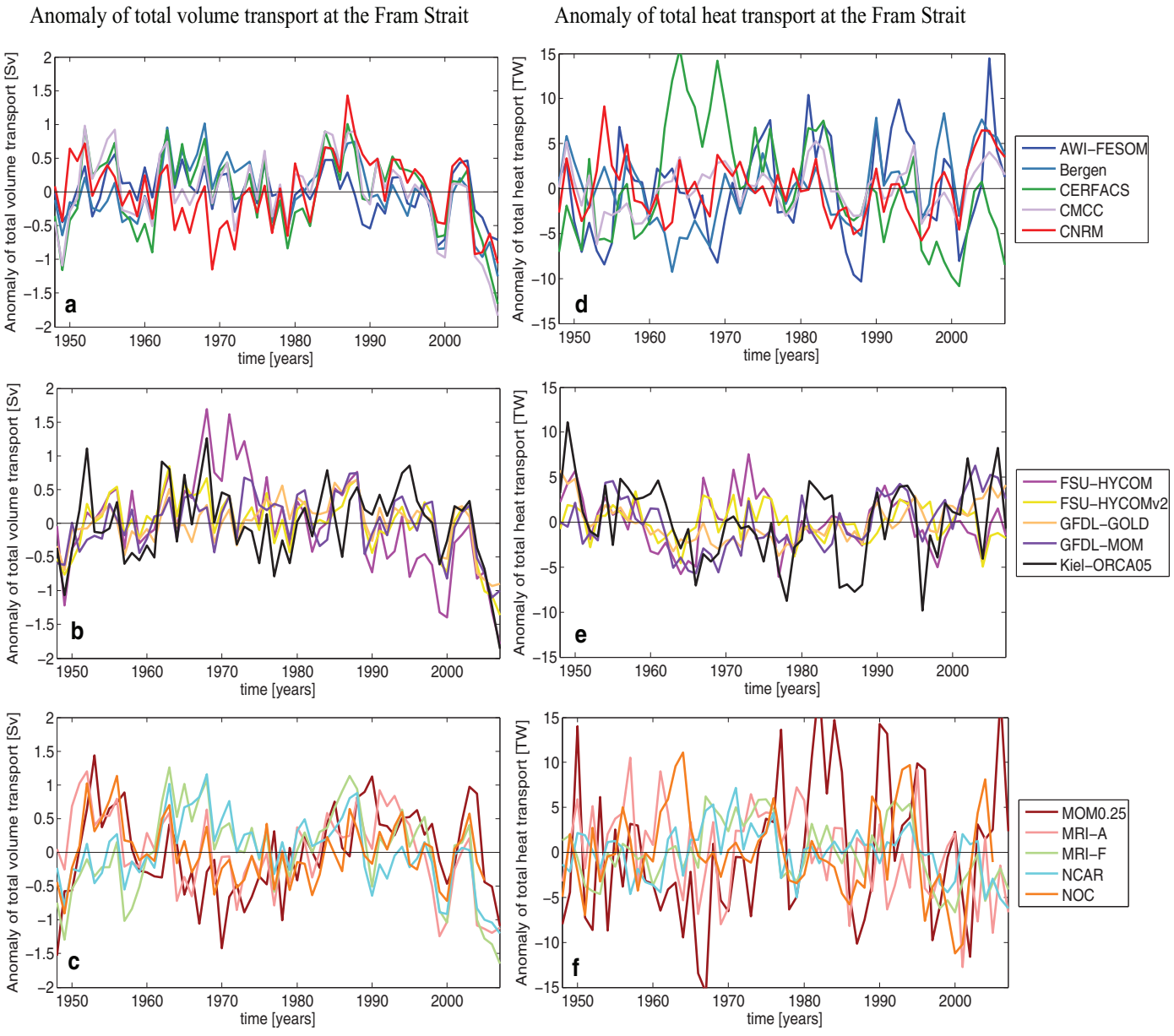

Fig. 14. Left: Anomaly of annual volume transport across the Fram Strait, unit is Sv. Right: Anomaly of annual heat transport across the Fram Strait, unit is TW.

Table 5
The mean Fram Strait net volume and heat transports and the standard deviation of the annual mean time series. Positive values indicate flux into the Arctic Ocean. The last 60 model years (1948–2007) are used in the analysis. The observed values are based on transports provided by Schauer et al. (2008). MMM is the multi model mean.

Model	Mean volume transport [Sv]	Standard deviation [Sv]	Mean heat transport [TW]	Standard deviation [TW]
Observed	−2.0 ± 2.7	0.3–0.47	26–50	
AWI-FESOM	−2.3	0.36	20.05	5.33
Bergen	−1.35	0.51	16.33	3.96
CERFACS	−2.35	0.56	17.46	6.38
CMCC	−2.71	0.58	18.14	2.47
CNRM	−3.49	0.54	22.91	3.05
FSU-HYCOM	−2.32	0.74	28.35	3.01
FSU-HYCOMv2	0.23	0.44	18.13	2.01
GFDL-GOLD	−2.11	0.37	22.06	1.93
GFDL-MOM	−2.19	0.43	28.65	3.08
Kiel-ORCA05	−1.55	0.57	21.75	4.2
MOM0.25	−1.13	0.61	44.02	8.17
MRI-A	−2.94	0.57	13.82	4.94
MRI-F	−3.63	0.66	27.82	3.55
NCAR	−0.69	0.54	14.55	2.99
NOC	−1.90	0.36	22.05	4.92
MMM	−1.95	1.12	22.98	8.35

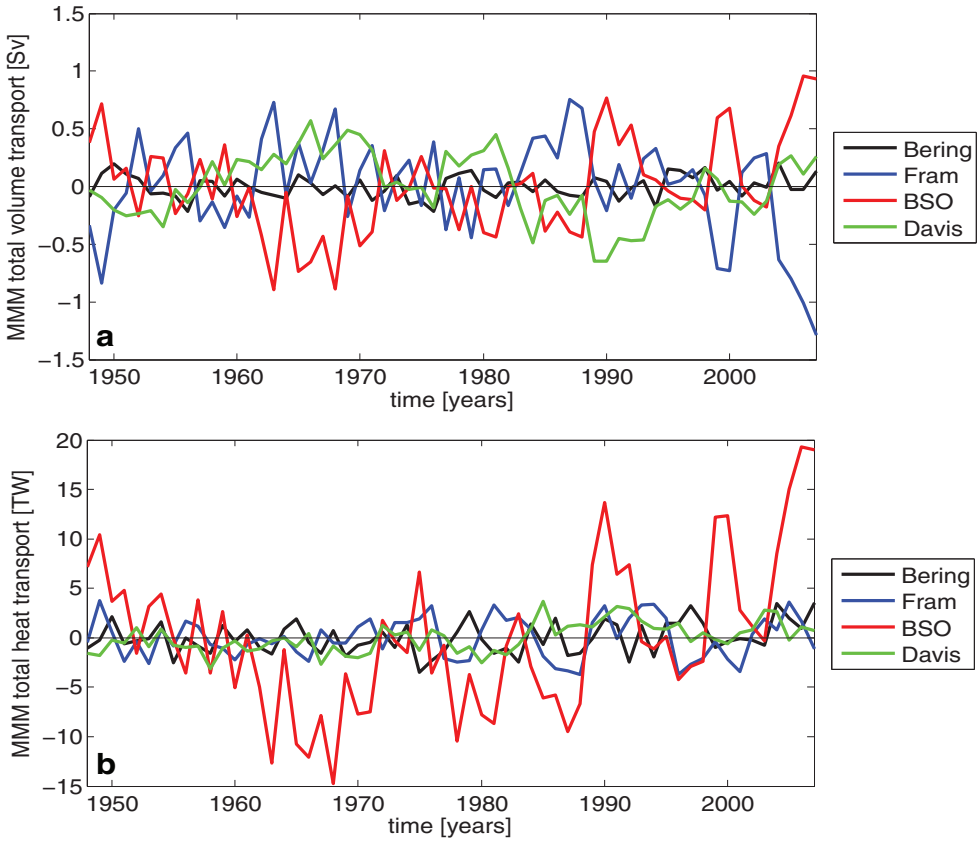

Fig. 15. Top: Anomaly of multi model mean annual volume transport across the Arctic gateways, unit is Sv. Bottom: Anomaly of multi model mean annual heat transport across the Arctic gateways, unit is TW.

the various models may not simulate similar interannual variations in the northward and southward volume and heat transports.

Some of the temporal variations are, however, consistent across the models. For instance, the models generally agree on a decline in the total transport between 1957 and 1961, and after 1988. The models do not necessarily agree on the reason for this drop. For the 1957–61 drop, NCAR simulates a decreasing northward transport while the southward transport is steady. On the other hand, the northward volume transport is steady in MRI-F with the decline caused by a reduced southward transport. For the post 1988 drop, Kiel-ORCA05, AWI-FESOM, FSU-HYCOM and GFDL-MOM show steady or increasing northward flows, whereas the remaining models show decreasing northward flows (not shown). It should also be mentioned that NCAR shows very low (2–3 Sv) northward and southward volume transports. Further investigation is required to examine the underlying mechanisms for the somewhat diverging transports among the CORE-II models in the Fram Strait.

The temporal evolution of anomalous annual heat transports at the Fram Strait are shown in Fig. 14. Available observation-based estimates indicate a northward heat transport across the Fram Strait between 26 and 50 TW (relative to 0 °C) for the time period 1997–2006, without any significant trend (Schauer et al., 2008).

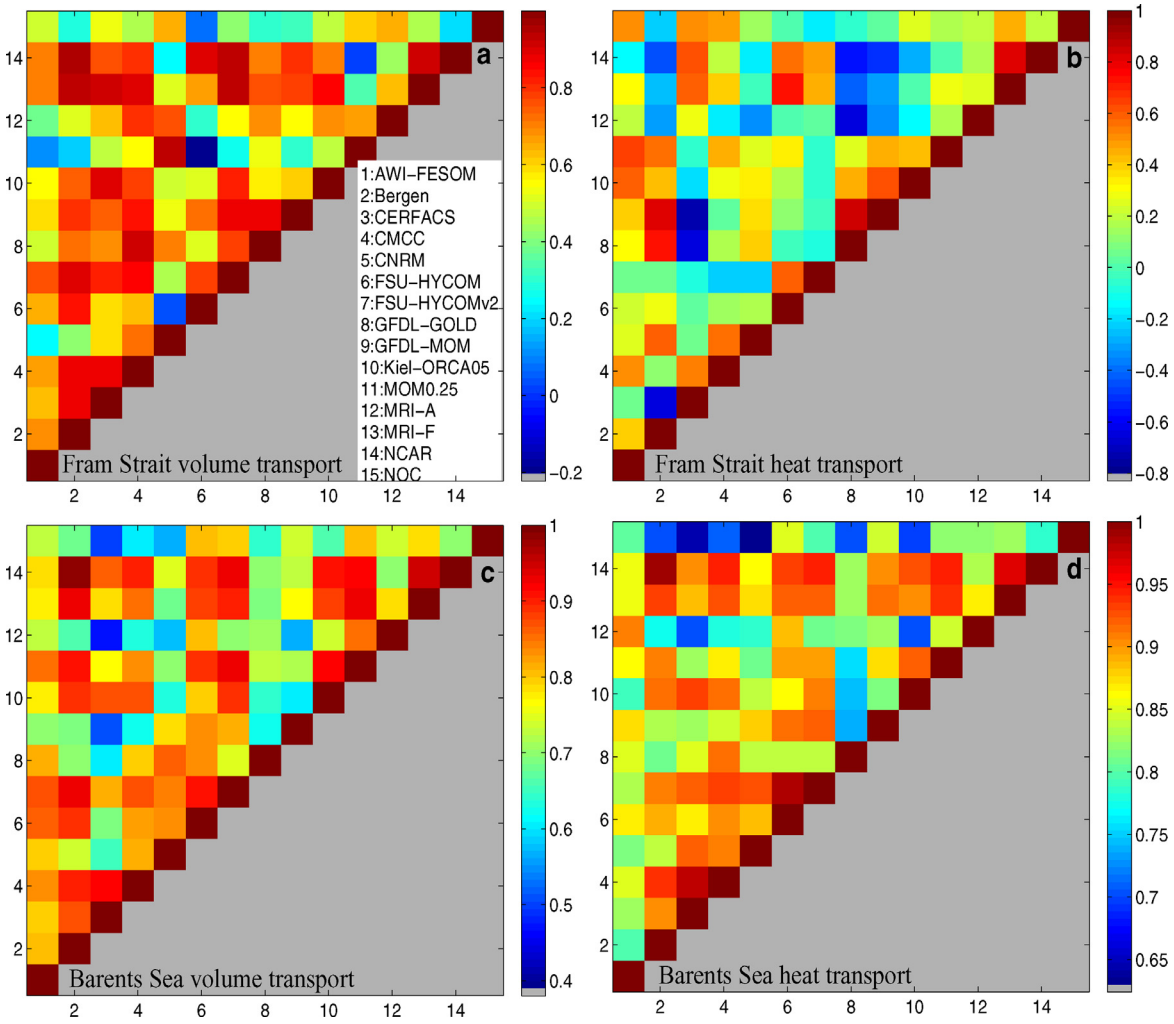

Fig. 16. (a, b) Model–model correlations for the volume and heat transport time series at the Fram Strait. (c, d) Model–model correlations for the volume and heat transport time series at the Barents Sea Opening. Low-pass filtered and mean removed. A 7-year cutoff is used for the filters. Note that different color ranges are used.

The multi model mean heat transport at the Fram Strait of 22.98 TW is thus at the lower end of the observation-based estimate.

A decreasing trend in the heat transport is found in CERFACS and possibly in NCAR as well. Although NCAR has a strong warm bias, it still has reasonable heat transport at the Fram Strait (≈14.5 TW). This raises a question: How can the heat transport be reasonable in warm-biased models? There might be two reasons for this; (i) the weak northward and southward volume transports in these models (low volume transports compensates for strong temperature biases); and (ii) the vertical gradient of temperature.

The other warm-biased models (i.e., GFDL-MOM, FSU-HYCOM and MRI-F) have around 28 TW mean heat transport which is consistent with the observation-based heat transport estimate. Across all models, MOM-0.25 has the strongest averaged heat transport of approximately 44 TW. The NEMO-based models and AWI-FESOM have all mean heat transports of ≈20 TW. Likewise, the models with very prominent cold biases, CNRM, BERGEN and GFDL-GOLD, have mean heat transports that are not systematically different from the other models.

By examining directional components of heat transport at the Fram Strait (not shown), two groups of models are identified based on the southward heat transport: the first group consists of models with negative southward heat transports (MRI-A, MRI-F, NCAR, AWI-FESOM). The exported temperature across the Fram Strait is above 0 °C in these models (warm-biased models). The second group has a positive southward heat transport with the mean southward temperature below 0 °C (cold-biased models).

Fig. 15 shows anomalies of the MMM volume and heat transports at the Arctic gateways. Compensation of volume transports between the Fram Strait and the Barents Sea Opening is clearly visible in Fig. 15(a). The mean multi model volume transport anomalies exhibit similar decadal variations to those seen in the individual models especially for the Fram and Davis Straits and BSO. The variation in the volume transport is clearly smallest for the shallow Bering Strait, as expected.

The most striking feature in the MMM heat transport anomalies is the clearly increasing signal at BSO (Fig. 15(b)). Note that heat transport to the Arctic Ocean is maximum at this gate (54 TW at BSO compared to 40 TW in total for the other gates). The leading role of the BO heat transport implies an increased ocean input of heat to the Arctic Ocean since the 1970s. The decreasing heat input to the Arctic Ocean from 1948 towards the end of the 1960s might be a consequence of the cyclic spin-up of the models (He et al., 2016).

5.6. Transport variability between models

A more quantitative assessment of the agreements and disagreements among the models in their representation of the heat and volume transports at the FS and BSO sections is provided in

Fig. 16, considering model-model correlations of the anomalous (mean removed) low-pass filtered transport time series discussed above. We use a Butterworth filter with the same cutoff period of 7 years used in Danabasoglu et al. (2016) to decompose the time series into their high and low-frequency components.

Fig. 16 (a) and (b) shows the low-pass filtered volume and heat transport time series correlations between the models at FS. For the volume transport, the majority of the models are in agreement in their representations of decadal variations. MOM-0.25 is the major outlier at this section, followed by NOC. Most of the models show high correlations in volume transports at BSO (Fig. 16(c)). Compared to the volume transports, the heat transports show generally lower correlations across the two sections (Fig. 16(b) and (d)). The latter is likely caused by differences in the mean state hydrography between the models.

6. Summary and conclusions

Simulations from 15 state-of-the-art ocean–sea ice models driven by the CORE-II forcing protocol are analyzed. The main focus is on the water masses, circulation features and fluxes into/out of the Arctic Ocean. Although all models are initialized from similar ocean states and are driven by the same atmospheric forcing state, we found that the models performed differently and had different biases in terms of hydrography in the Arctic Ocean mean state.

There is a large spread in temperature in the Arctic Ocean between the models, and also generally large differences compared to the PHC3.0 observation-based temperature. Many of the CORE-II models either have clearly warm (e.g., NCAR, GFDL-MOM, MOM-0.25, FSU-HYCOM and FSU-HYCOMv2) or cold (CNRM, Kiel-ORCA05,BERGEN, GFDL-GOLD and CMCC) biases in the interior of the Arctic. Two physical processes are behind these temperature biases. The first factor is that AW is either warmer and more widely spread or colder/less present in many of the models. Warm bias models have, for instance, a strongly positive temperature anomaly associated with the AW entering the Arctic Ocean through FS. The second factor is the volume and transport of cold and dense waters formed on the eastern shelves in the models. In the cold bias models, excessive cold water forms in the Barents Sea. This cold water flows as a gravity current through the St. Anna Trough and erodes the Atlantic layer in the Eurasian Basin. Similarly, lack of deep water formation and/or transport through the St. Anna Trough is clearly visible in the warm bias models. Note that observations indicate a St. Anna Trough volume transport of approximately 1 Sv (Rudels et al., 2013). For comparison, the Mediterranean overflow has a mean transport of 0.7 Sv, spreading over large parts of the North Atlantic Ocean. Thus, to accurately model the gravity currents in the relatively small Arctic Ocean domain is an issue of prime importance. Furthermore, all models are saltier than the PHC3.0 climatology in the upper 50 m of the Eurasian Basin. Below 50 m, only NCAR stays saltier than the observed, vertical salinity field.

There is a large spread in the simulated mean transport through FS and BSO. The models agree more on the decadal variations, to a large degree dictated by the common atmospheric forcing. For the latter, the Fram Strait and BSO volume transports are negatively correlated. Since the mid-1990s, the MMM volume transport has decreased in the Fram Strait and increased in the BSO. For the MMM heat transports (relative to 0 °C), the decadal-scale variations are mainly governed by variations in BSO. For the latter, a positive trend is obtained starting from the early 1970s, implying a net advective input of heat into the Barents Sea, but not necessarily into the Arctic Basin due to the strong winter cooling in the shallow Barents Sea.

We conclude that the CORE-II model study provides guidance to understand the crucial biases in the Arctic Ocean. However, further investigations are needed to identify and resolve the issues related to these biases. For instance, poor representation of the North Atlantic Inflow can be due to subduction mechanisms in the Svalbard region or to flow and/or hydrographic biases in the Norwegian Atlantic Current. The latter might be caused by unrealistic circulation or representation of processes in the North Atlantic, far upstream of the Nordic Seas/Arctic Ocean (e.g., Hátún et al., 2005). The cold water overflow being guided by the St. Anna Trough is not well represented in the ocean components of the current climate models. This can be due to unrealistic formation rates of dense water masses on the shelves, the actual representation of the bathymetry, different sea-ice models, lack of diapycnal mixing in isopycnic models or excessive spurious mixing in geopotential coordinate models.

Improved representation of the Arctic Ocean, both its mean state and its variability, is likely as important for interannual-to-decadal predictions (Goddard et al., 2013) as for climate projections. Although the CORE-II family of models show similarities in the (temporal) ocean response to the prescribed CORE-II forcing, this might be very different in a fully coupled system, particularly for the Arctic Ocean with tightly coupled and highly non-linear heat and momentum fluxes at the air–sea ice–ocean interface.

We should emphasize that some CORE-II models exhibit similar biases in the Arctic Ocean in their respective coupled climate models but other models do not. For example, the fully coupled version of NCAR has the same warm bias and lack of deep water formation on the shelves to the CORE-II setup (Danabasoglu et al., 2012). However, the fully coupled CMIP5 version of BERGEN has less cold bias in the Arctic interior compared to the CORE-II version (Bentsen et al., 2012). For BERGEN, this might be due to the actual grid setup since the rest of the model parameterizations are unchanged. In the CMIP5 version, this model employs bipolar grid whereas in the CORE-II simulations, tripolar grid has been used.

The accompanying papers by Wang et al. 2016a; 2016b and the Southern Ocean analysis of the CORE-II simulations by Downes et al. (2015) and Farneti et al. (2015) illuminate the status of current state-of-the-art ocean models in simulating the high-latitude oceans. Despite the relatively small area of the polar regions, particularly for the Arctic Ocean, these regions form an important part of the global climate system, and thus for climate simulations of the past, present and possible future climate states. It is our intention that the reported deficiencies and model spread might guide forthcoming research, and eventually provide improved ocean and sea-ice components in coupled climate models. One direct avenue in this respect would be to explore the extent to which current state-of-the-art ocean models improve with increasing spatial resolution.

Acknowledgments

M. Ilicak is supported by Ice2Ice project that has received funding from the European Research Council under the European Community's Seventh Framework Programme (FP7/2007-2013)/ERC grant agreement no. 610055.

M. Bentsen, H. Drange and M. Ilicak acknowledge support from the Research Council of Norway through the project EVA (grants 229771, nn2345k, ns2345k).

The WCRP/CLIVAR Ocean Model Development Panel (OMDP) is responsible for organizing the Coordinated Ocean-sea ice Reference Experiments, with support from the international CLIVAR and U.S. CLIVAR project offices. We are grateful for the efforts of modelers who have contributed to the simulation and processing of the CORE-II experiments.

The BERGEN contribution is supported by the Research Council of Norway through the EarthClim (207711/E10) and NOTUR/NorStore projects, as well as the Centre for Climate Dynamics at the Bjerknes Centre for Climate Research.

AWI is a member of the Helmholtz Association of German Research Centers. Q. Wang is funded by the Helmholtz Climate Initiative REKLIM (Regional Climate Change) project.

The CMCC contribution received funding from the Italian Ministry of Education, University, and Research and the Italian Ministry of Environment, Land, and Sea under the GEMINA project.

NCAR is sponsored by the U.S. National Science Foundation (NSF). S.G. Yeager was supported by the NOAA Climate Program Office under Climate Variability and Predictability Program grants NA09OAR4310163 and NA13OAR4310138 and by the NSF Collaborative Research EaSM2 grant OCE-1243015 to NCAR.

The GEOMAR experiments were performed at the North-German Supercomputing Alliance (HLRN). C. Roth was supported by the Co-Operative Project "RACE-Regional Atlantic Circulation and Global Change" funded by the German Federal Ministry for Education and Research (BMBF), grant no. 03F0651B.

The NOC contribution was partly supported by the UK Natural Environment Research Council (NERC) Marine Centres – Strategic Research Programme and partly by the Arctic Research Programme TEA-COSI project (NE/I028947/1). We also acknowledge the annual meetings of the Forum for Arctic Modeling and Observing Synthesis (FAMOS), funded by the National Science Foundation Office of Polar Programs, awards PLR-1313614 and PLR-1203720 being instrumental in conceiving ideas and in inspiring the present study and are thankful to FAMOS for travel support to attend these meetings. The NOC-ORCA simulations were performed using the NOC local computing facilities and the cluster MOBILIS.

P. Spence is supported by the Australian Research Council grant DE150100223.

We also thank three anonymous reviewers for their constructive comments, which helped us to improve the manuscript.

Supplementary material

Supplementary material associated with this article can be found, in the online version, at 10.1016/j.ocemod.2016.02.004.

References

ACIA, 2005. Arctic Climate Impact Assessment. Cambridge University Press.

Applegate, P.J., Parizek, B.R., Nicholas, R.E., Alley, R.B., Keller, K., 2014. Increasing temperature forcing reduces the greenland ice sheet's response time scale. Clim. Dyn 45 (7), 2001–2011.

Barrier, N., Deshayes, J., Treguier, A.-M., Cassou, C., 2015. Heat budget in the North Atlantic subpolar gyre: impacts of atmospheric weather regimes on the 1995 warming event. Prog. Oceanogr. 130, 75–90. doi:10.1016/j.pocean.2014.10.001.

Bentsen, M., Bethke, I., Debernard, J.B., Iversen, T., Kirkevåg, A., Seland, Ø., Drange, H., Roelandt, C., Seierstad, I.A., Hoose, C., Kristjánsson, J.E., 2012. The Norwegian Earth System Model, NorESM1-M. Part 1. Description and basic evaluation. Geosci. Model Dev. Discuss. 5, 2843–2931. doi:10.5194/gmdd-5-2843-2012.

Bezczynska-Möller, A., Woodgate, R., Lee, C., Melling, H., Karcher, M., 2011. A synthesis of exchanges through the main oceanic gateways to the arctic ocean. Oceanography 24, 82–99.

Blindheim, J., 1989. Cascading of barents sea bottom water into the Norwegian sea. Rapp. P.-v. Reun. Cons. int. Explor. Mer 188, 49–58.

Blüthgen, J., Gerdes, R., Werner, M., 2012. Atmospheric response to the extreme Arctic sea ice conditions in 2007. Geophys. Res. Lett. 39, L02707. doi:10.1029/2011GL050486.

Cohen, J., Screen, J.A., Furtado, J.C., Barlow, M., Whittleston, D., Coumou, D., Francis, J., Dethloff, K., Entekhabi, D., Overland, J., Jones, J., 2014. Recent arctic amplification and extreme mid-latitude weather. Nat. Geosci. 7, 627–637.

Cuny, J., Rhines, P., Ronkwok, 2005. Davis Strait volume, freshwater and heat fluxes. Deep Sea Res. Part II: Top. Stud. Oceanogr. 52, 519–542. doi:10.1016/j.dsr.2004.10.006.

Curry, B., Lee, C., Petrie, B., Moritz, R.E., Kwok, R., 2014. Multiyear volume, liquid freshwater, and sea ice transports through Davis Strait, 2004–2010. J. Phys. Oceanogr. 44, 1244–1266.

Curry, B., Lee, C.M., Petrie, B., 2011. Volume, freshwater, and heat fluxes through Davis Strait, 2004–05*. J. Phys. Oceanogr. 41, 429–436. doi:10.1175/2010JPO4536.1.

Danabasoglu, G., Bates, S.C., Briegleb, B.P., Jayne, S.R., Jochum, M., Large, W.G., Peacock, S., Yeager, S.G., 2012. The CCSM4 ocean component. J. Clim. 25, 1361–1389. doi:10.1175/JCLI-D-11-00091.1.

Danabasoglu, G., Yeager, S.G., Bailey, D., Behrens, E., Bentsen, M., Bi, D., Biastoch, A., Böning, C., Bozec, A., Canuto, V.M., Cassou, C., Chassignet, E., Coward, A.C., Danilov, S., Diansky, N., Drange, H., Farneti, R., Fernandez, E., Fogli, P.G., Forget, G., Fujii, Y., Griffies, S.M., Gusev, A., Heimbach, P., Howard, A., Jung, T., Kelley, M., Large, W.G., Leboissetier, A., Lu, J., Madec, G., Marsland, S.J., Masina, S., Navarra, A., George Nurser, A.J., Pirani, A., y Mélia, D.S., Samuels, B.L., Scheinert, M., Sidorenko, D., Treguier, A.-M., Tsujino, H., Uotila, P., Valcke, S., Voldoire, A., Wang, Q., 2014. North Atlantic simulations in coordinated ocean-ice reference experiments phase II (CORE-II). Part I. Mean states. Ocean Modell. 73, 76–107. doi:10.1016/j.ocemod.2013.10.005.

Danabasoglu, G., Yeager, S.G., Kim, W.M., Behrens, E., Bentsen, M., Bi, D., Biastoch, A., Bleck, R., Böning, C., Bozec, A., Canuto, V.M., Cassou, C., Chassignet, E., Coward, A.C., Danilov, S., Diansky, N., Drange, H., Farneti, R., Fernandez, E., Fogli, P.G., Forget, G., Fujii, Y., Griffies, S.M., Gusev, A., Heimbach, P., Howard, A., Jung, T., Kelley, M., Large, W.G., Leboissetier, A., Lu, J., Madec, G., Marsland, S.J., Masina, S., Navarra, A., George Nurser, A.J., Pirani, A., Romanou, A., y Mélia, D.S., Samuels, B.L., Scheinert, M., Sidorenko, D., Sun, S., Treguier, A.-M., Tsujino, H., Uotila, P., Valcke, S., Voldoire, A., Wang, Q., 2016. North Atlantic simulations in coordinated ocean-ice reference experiments phase II (CORE-II). Part II. Interannual to decadal variability. Ocean Modell. 97, 65–90. (in press).

Dickson, R.R., Osborn, T.J., Hurrell, J.W., Meincke, J., Blindheim, J., Adlandsvik, B., Vinje, T., Alekseev, G., Maslowski, W., 2000. The Arctic Ocean response to the North Atlantic oscillation. J. Clim. 13, 2671–2696. doi:10.1175/1520-0442(2000)013⟨2671:TAORTT⟩2.0.CO;2.

Downes, S.M., Farneti, R., Uotila, P., Griffies, S.M., Marsland, S.J., Bailey, D., Behrens, E., Bentsen, M., Bi, D., Biastoch, A., Böning, C., Bozec, A., Canuto, V.M., Chassignet, E., Danabasoglu, G., Danilov, S., Diansky, N., Drange, H., Fogli, P.G., Gusev, A., Howard, A., Ilicak, M., Jung, T., Kelley, M., Large, W.G., Leboissetier, A., Long, M., Lu, J., Masina, S., Mishra, A., Navarra, A., George Nurser, A.J., Patara, L., Samuels, B.L., Sidorenko, D., Spence, P., Tsujino, H., Wang, Q., Yeager, S.G., 2015. An assessment of Southern Ocean water masses and sea ice during 1988–2007 in a suite of interannual CORE-II simulations. Ocean Modell. 94, 67–94.

Eldevik, T., Nilsen, J.E.Ø., 2013. The Arctic-Atlantic thermohaline circulation. J. Clim. 26, 8698–8705. doi:10.1175/JCLI-D-13-00305.1.

Farneti, R., Downes, S.M., Griffies, S.M., Marsland, S.J., Behrens, E., Bentsen, M., Bi, D., Biastoch, A., Böning, C., Bozec, A., Canuto, V.M., Chassignet, E., Danabasoglu, G., Danilov, S., Diansky, N., Drange, H., Fogli, P.G., Gusev, A., Hallberg, R.W., Howard, A., Ilicak, M., Jung, T., Kelley, M., Large, W.G., Leboissetier, A., Long, M., Lu, J., Masina, S., Mishra, A., Navarra, A., George Nurser, A.J., Patara, L., Samuels, B.L., Sidorenko, D., Tsujino, H., Uotila, P., Wang, Q., Yeager, S.G., 2015. An assessment of Antarctic circumpolar current and southern ocean meridional overturning circulation during 1958–2007 in a suite of interannual CORE-II simulations. Ocean Modell. 93, 84–120.

Fieg, K., Gerdes, R., Fahrbach, E., Beszczynska-Möller, A., Schauer, U., 2010. Simulation of oceanic volume transports through Fram Strait 1995–2005. Ocean Dyn. 60, 491–502.

Flato, G., Marotzke, J., Abiodun, B., Braconnot, P., Chou, S., Collins, W., Cox, P., Driouech, F., Emori, S., Eyring, V., Forest, C., Gleckler, P., Guilyardi, E., Jakob, C., Kattsov, V., Reason, C., Rummukainen, M., 2013. Evaluation of climate models. Climate Change 2013: The Physical Science Basis. Contribution of Working Group I to the Fifth Assessment Report of the Intergovernmental Panel on Climate Change. Cambridge University Press.

Gent, P.R., McWilliams, J.C., 1990. Isopycnal mixing in ocean circulation models. J. Phys. Oceanogr. 20, 150–160. doi:10.1175/1520-0485(1990)020⟨0150:IMIOCM⟩2.0.CO;2.

Goddard, L., Kumar, A., Solomon, A., Smith, D., Boer, G., Gonzalez, P., Kharin, V., Merryfield, W., Deser, C., Mason, S.J., Kirtman, B.P., Msadek, R., Sutton, R., Hawkins, E., Fricker, T., Hegerl, G., Ferro, C.A.T., Stephenson, D.B., Meehl, G.A., Stockdale, T., Burgman, R., Greene, A.M., Kushnir, Y., Newman, M., Carton, J., Fukumori, I., Delworth, T., 2013. A verification framework for interannual-to-decadal predictions experiments. Clim. Dyn. 40, 245–272. doi:10.1007/s00382-012-1481-2.

Griffies, S.M., Biastoch, A., Böning, C., Bryan, F., Danabasoglu, G., Chassignet, E.P., England, M.H., Gerdes, R., Haak, H., Hallberg, R.W., Hazeleger, W., Jungclaus, J., Large, W.G., Madec, G., Pirani, A., Samuels, B.L., Scheinert, M., Gupta, A.S., Severijns, C.A., Simmons, H.L., Treguier, A.M., Winton, M., Yeager, S., Yin, J., 2009. Coordinated ocean-ice reference experiments (CORes). Ocean Modell. 26, 1–46. doi:10.1016/j.ocemod.2008.08.007.

Griffies, S.M., Pacanowski, R.C., Hallberg, R.W., 2000. Spurious diapycnal mixing associated with advection in a z-coordinate ocean model. Mon. Wea. Rev. 128, 538–564. doi:10.1175/1520-0493(2000)128⟨0538:SDMAWA⟩2.0.CO;2.

Griffies, S.M., Winton, M., Samuels, B., Danabasoglu, G., Yeager, S.G., Marsland, S., Drange, H., Bentsen, M., 2012. Datasets and protocol for the CLIVAR WGOMD coordinated ocean-sea ice reference experiments (CORes). Technical Report 21. WCRP Report. WCRP.

Haine, T.W., Curry, B., Gerdes, R., Hansen, E., Karcher, M., Lee, C., Rudels, B., Spreen, G., de Steur, L., Stewart, K.D., Woodgate, R., 2015. Arctic freshwater export: Status, mechanisms, and prospects. Glob. Planet. Change 125, 13–35.

Hátún, H., Sandø, A.B., Drange, H., Hansen, B., Valdimarsson, H., 2005. Influence of the Atlantic subpolar gyre on the thermohaline circulation. Science 309, 1841–1844. doi:10.1126/science.1114777.

He, Y.C., Drange, H., Gao, Y., Bentsen, M., 2016. Simulated Atlantic Meridional Overturning Circulation in the 20th century with an ocean model forced by reanalysis-based atmospheric data. sets. Ocean Modell. 100, 31–48.

Hinzman, L.D., Deal, C.J., McGuire, A.D., Mernild, S.H., Polyakov, I.V., Walsh, J., 2013. Trajectory of the Arctic as an integrated system. Ecol. Appl. 23, 1837–1868.

Holloway, G., Dupont, F., Golubeva, E., Häkkinen, S., Hunke, E., Jin, M., Karcher, M., Kauker, F., Maltrud, M., Morales Maqueda, M.A., Maslowski, W., Platov, G., Stark, D., Steele, M., Suzuki, T., Wang, J., Zhang, J., 2007. Water properties and circulation in Arctic Ocean models. J. Geophys. Res.: Oceans 112, 4. doi:10.1029/2006JC003642.

Ilıcak, M., Adcroft, A.J., Griffies, S.M., Hallberg, R.W., 2012. Spurious dianeutral mixing and the role of momentum closure. Ocean Modell. 45, 37–58. doi:10.1016/j.ocemod.2011.10.003.

Jahn, A., Aksenov, Y., de Cuevas, B.A., de Steur, L., Häkkinen, S., Hansen, E., Herbaut, C., Houssais, M.-N., Karcher, M., Kauker, F., Lique, C., Nguyen, A., Pemberton, P., Worthen, D., Zhang, J., 2012. Arctic Ocean freshwater: How robust are model simulations? J. Geophys. Res.: Oceans 117, C00D16. doi:10.1029/2012JC007907.

Jones, E., 2001. Circulation in the Arctic Ocean. Polar Res. 20, 139–146.

Karcher, M., Kauker, F., Gerdes, R., Hunke, E., Zhang, J., 2007. On the dynamics of Atlantic Water circulation in the Arctic Ocean. J. Geophys. Res.: Oceans 112, 4. doi:10.1029/2006JC003630.

Koenig, S.J., DeConto, R.M., Pollard, D., 2014. Impact of reduced arctic sea ice on greenland ice sheet variability in a warmer than present climate. Geophys. Res. Lett. 41, 3934–3943.

Kug, J.S., Jeong, J.H., Jang, Y.S., Kim, B.M., Folland, C.K., Min, S.K., Son, S.W., 2015. Two distinct influences of Arctic warming on cold winters over North America and East Asia. Nat. Geosci. 8, 759–762.

Large, W.G., Yeager, S.G., 2009. The global climatology of an interannually varying air-sea flux data set. Clim. Dyn. 33, 341–364.

Levitus, S., Boyer, T., Concright, M., Johnson, D., O'Brien, T., Antonov, J., Stephens, C., Garfield, R., 1998. World Ocean Database 1998. Vol. I: Introduction. NOAA Atlas NESDIS, vol. 18. U.S. Government Printing Office, Washington, D.C., p. 346.

Marshall, D., 1997. Subduction of water masses in an eddying ocean. J. Mar. Res. 55, 201–222.

Mauritzen, C., 1996. Production of dense overflow waters feeding the north atlantic acrosshe greenland-scotland ridge, 1, evidence for a revised circulation scheme. Deep Sea Res. 43, 769–806.

McClelland, J.W., Déry, S.J., Peterson, B.J., Holmes, R.M., Wood, E.F., 2006. A pan-arctic evaluation of changes in river discharge during the latter half of the 20th century. Geophys. Res. Lett. 33, 6715. doi:10.1029/2006GL025753.

McGeehan, T., Maslowski, W., 2012. Evaluation and control mechanisms of volume and freshwater export through the Canadian Arctic Archipelago in a high-resolution pan-Arctic ice-ocean model. J. Geophys. Res.: Oceans 117, C00D14. doi:10.1029/2011JC007261.

Midttun, L., 1985. Formation of dense bottom water in the barents sea. Deep-Sea Res. 32, 1233–1241.

Mori, M., Watanabe, M., Shiogama, H., Inoue, J., Kimoto, M., 2014. Robust arctic sea-ice influence on the frequent eurasian cold winters in past decades. Nat. Geosci. 7, 869–873.

Nguyen, A.T., Menemenlis, D., Kwok, R., 2009. Improved modeling of the Arctic halocline with a subgrid-scale brine rejection parameterization. J. Geophys. Res.: Oceans 114, 11014. doi:10.1029/2008JC005121.

Nurser, A.J.G., Bacon, S., 2014. The Rossby radius in the Arctic Ocean. Ocean Sci. 10, 967–975. doi:10.5194/os-10-967-2014.

O'Connor, F.M., Boucher, O., Gedney, N., Jones, C.D., Folberth, G.A., Coppell, R., Friedlingstein, P., Collins, W.J., Chappellaz, J., Ridley, J., Johnson, C.E., 2010. Possible role of wetlands, permafrost, and methane hydrates in the methane cycle under future climate change: a review. Rev. Geophys. 48, RG4005. doi:10.1029/2010RG000326.

Orvik, K.A., 2002. Major pathways of atlantic water in the northern north atlantic and nordic seas toward Arctic. Geophys. Res. Lett. 29, 19.

Pemberton, P., Nilsson, J., Hieronymus, M., Meier, H.E.M., 2015. Arctic Ocean water mass transformation in S-T coordinates. J. Phys. Oceanogr. 45, 1025–1050. doi:10.1175/JPO-D-14-0197.1.

Peralta-Ferriz, C., Woodgate, R.A., 2014. Seasonal and interannual variability of pan-Arctic surface mixed layer properties from 1979 to 2012 from hydrographic data. Prog. Oceanogr 134, 19–53.

Peterson, B.J., Holmes, R.M., McClelland, J.W., Vörösmarty, C.J., Lammers, R.B., Shiklomanov, A.I., Shiklomanov, I.A., Rahmstorf, S., 2002. Increasing river discharge to the arctic ocean. Science 298, 2171–2173.

Peterson, I., Hamilton, J., Prinsenberg, S., Pettipas, R., 2012. Wind-forcing of volume transport through Lancaster Sound. J. Geophys. Res.: Oceans 117, 11018. doi:10.1029/2012JC008140.

Polyak, L., Alley, R.B., Andrews, J.T., Brigham-Grette, J., Cronin, T.M., Darby, D.A., Dyke, A.S., Fitzpatrick, J.J., Funder, S., Holland, M., Jennings, A.E., Miller, G.H., O'Regan, M., Savelle, J., Serreze, M., John, K.S., White, J.W., Wolff, E., 2010. History of sea ice in the Arctic. Q. Sci. Rev. 29, 1757–1778.

Polyakov, I.V., Walsh, J.E., Kwok, R., 2012. Recent changes of arctic multiyear sea ice coverage and the likely causes. Bull. Am. Meteor. Soc. 93, 145–151.

Prather, M., 1986. Numerical advection by conservation of second-order moments. J. Geophys. Res. 91, 6671–6681.

Price, J.F., 2001. Subduction. In: Siedler, G., Church, J., Gould, J. (Eds.), Ocean Circulation and Climate. In: International Geophysics Series. Academic Press, pp. 357–372.

Proshutinsky, A., Kowalik, Z., 2007. Preface to special section on Arctic ocean model intercomparison project (AOMIP) studies and results. J. Geophys. Res.: Oceans 112, 4. doi:10.1029/2006JC004017.

Proshutinsky, A.Y., Timmermans, M.E., Krishfield, R.A., Toole, J.M., 2011. The role of the Beaufort Gyre in the Arctic climate system changes. AGU Fall Meeting Abstracts, p. A27.

Roach, A.T., Aagaard, K., Pease, C.H., Salo, S.A., Weingartner, T., Pavlov, V., Kulakov, M., 1995. Direct measurements of transport and water properties through the Bering Strait. J. Geophys. Res.: Oceans 100, 18443. doi:10.1029/95JC01673.

Rudels, B., 1987. On the mass balance of the Polar Ocean, with special emphasis on the Fram Strait. Nor. Polarinst Skr. 188, 53.

Rudels, B., 2012. Arctic ocean circulation and variability – advection and external forcing encounter constraints and local processes. Ocean Sci. 8, 261–286.

Rudels, B., 2015. Arctic Ocean circulation, processes and water masses: a description of observations and ideas with focus on the period prior to the International Polar Year 2007-2009. Prog. Oceanogr. 132, 22–67. doi:10.1016/j.pocean.2013.11.006.

Rudels, B., Jones, E.P., Anderson, L.G., Kattner, G., 1994. On the Intermediate Depth Waters of the Arctic Ocean. In: Geophysical Monograph Series, vol. 85. American Geophysical Union, Washington, DC, pp. 33–46. doi:10.1029/GM085p0033.

Rudels, B., Schauer, U., Björk, G., Korhonen, M., Pisarev, S., Rabe, B., Wisotzki, A., 2013. Observations of water masses and circulation with focus on the Eurasian Basin of the Arctic Ocean from the 1990s to the late 2000s. Ocean Sci. 9, 147–169. doi:10.5194/os-9-147-2013.

Schauer, U., Beszczynska-Möller, A., Walczowski, W., Fahrbach, E., Piechura, J., Hansen, E., 2008. Variation of measured heat flow through the fram strait between 1997 and 2006. In: Dickson, B., Meincke, J., Rhines, P. (Eds.), In: Arctic-Subarctic Ocean Fluxes: Defining the Role of Nordic Seas in Climate. Springer, Berlin. (Chapter 3).

Schmidtko, S., Johnson, G.C., Lyman, J.M., 2013. MIMOC: a global monthly isopycnal upper-ocean climatology with mixed layers. J. Geophys. Res.: Oceans 118, 1658–1672. doi:10.1002/jgrc.20122.

Skagseth, Ø., Furevik, T., Ingvaldsen, R., Loeng, H., Mork, K.A., Orvik, K.A., Ozhigin, V., 2008. Volume and heat transports to the Arctic Ocean via the Norwegian and Barents Seas. In: Dickson, B., Meincke, J., Rhines, P. (Eds.), In: Arctic-Subarctic Ocean Fluxes: Defining the Role of Nordic Seas in Climate. Springer, Berlin. (Chapter 2).

Skogseth, R., Haugan, P., Jakobsson, M., 2005. Watermass transformations in storfjorden. Cont. Shelf Res. 25, 667–695.

Smedsrud, L.H., Esau, I., Ingvaldsen, R.B., Eldevik, T., Haugan, P.M., Li, C., Lien, V.S., Olsen, A., Omar, A.M., Otterå, O.H., Risebrobakken, B., Sandø, A.B., Semenov, V.A., Sorokina, S.A., 2013. The role of the Barents Sea in the Arctic climate system. Rev. Geophys. 51, 415–449. doi:10.1002/rog.20017.

Steele, M., Boyd, T., 1998. Retreat of the cold halocline layer in the Arctic ocean. J. Geophys. Res. 103, 10419–10435.

Steele, M., Morley, R., Ermold, W., 2001. PHC: a global ocean hydrography with a high-quality Arctic Ocean. J. Clim. 14, 2079–2087. doi:10.1175/1520-0442(2001)014⟨2079:PAGOHW⟩2.0.CO;2.

Timmermans, M.-L., Cole, S., Toole, J., 2012. Horizontal density structure and restratification of the Arctic Ocean surface layer. J. Phys. Oceanogr. 42, 659–668. doi:10.1175/JPO-D-11-0125.1.

Wallace, J.M., Held, I.M., Thompson, D.W.J., Trenberth, K.E., Walsh, J.E., 2014. Global warming and winter weather. Science 343, 729–730.

Wang, Q., Ilicak, M., et al., 2016a. An assessment of the Arctic Ocean in a suite of 1239 interannual CORE-II simulations. Part I. Sea ice and solid freshwater, Ocean Modelling 99, 110–132.

Wang, Q., Ilicak, M., et al., 2016b. An assessment of the Arctic Ocean in a suite of 1239 interannual CORE-II simulations. Part II. Liquid freshwater. Ocean Modell. 99, 86–109.

Woodgate, R.A., Aagaard, K., 2005. Revising the Bering Strait freshwater flux into the Arctic Ocean. Geophys. Res. Lett. 32, L02602. doi:10.1029/2004GL021747.

Zhang, X., He, J., Zhang, J., Polyakov, I., Gerdes, R., Inoue, J., Wu, P., 2013. Enhanced poleward moisture transport and amplified northern high-latitude wetting trend. Nat. Clim. Change 3, 47–51.